

# High Nitrile Yields of Aerobic Ammoxidation of Alcohols Achieved by Generating $\bullet\text{O}_2^-$ and $\text{Br}\bullet$ Radicals over Iron-Modified $\text{TiO}_2$ Photocatalysts

Chensheng Xian,<sup>§</sup> Jie He,<sup>§</sup> Yurong He, Jiabao Nie, Ziliang Yuan, Jie Sun, Wayde N. Martens, Jingzhong Qin, Huai-Yong Zhu,<sup>\*</sup> and Zehui Zhang<sup>\*</sup>



Cite This: <https://doi.org/10.1021/jacs.2c07061>



Read Online

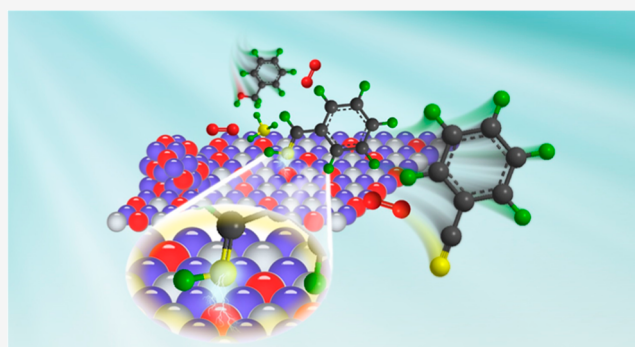
ACCESS |

Metrics & More

Article Recommendations

Supporting Information

**ABSTRACT:** Catalytic ammoxidation of alcohols into nitriles is an essential reaction in organic synthesis. While highly desirable, conducting the synthesis at room temperature is challenging, using  $\text{NH}_3$  as the nitrogen source,  $\text{O}_2$  as the oxidant, and a catalyst without noble metals. Herein, we report robust photocatalysts consisting of Fe(III)-modified titanium dioxide ( $\text{Fe}/\text{TiO}_2$ ) for ammoxidation reactions at room temperature utilizing oxygen at atmospheric pressure,  $\text{NH}_3$  as the nitrogen source, and  $\text{NH}_4\text{Br}$  as an additive. To the best of our knowledge, this is the first example of catalytic ammoxidation of alcohols over a photocatalyst using such cheap and benign materials. Various (hetero) aromatic nitriles were synthesized at high yields, and aliphatic alcohols could also be transformed into corresponding nitriles at considerable yields. The modification of  $\text{TiO}_2$  with Fe(III) facilitates the formation of active  $\bullet\text{O}_2^-$  radicals and increases the adsorption of  $\text{NH}_3$  and amino intermediates on the catalyst, accelerating the ammoxidation to yield nitriles. The additive  $\text{NH}_4\text{Br}$  impressively improves the catalytic efficiency *via* the formation of bromine radicals ( $\text{Br}\bullet$ ) from  $\text{Br}^-$ , which works synergistically with  $\bullet\text{O}_2^-$  to capture  $\text{H}\bullet$  from  $\text{C}_\alpha\text{-H}$ , which is present in benzyl alcohol and the intermediate aldimine ( $\text{RCH}=\text{NH}$ ), to generate the active carbon-centered radicals. Further, the generation of  $\text{Br}\bullet$  from the  $\text{Br}^-$  additive consumes the photogenerated holes and  $\text{OH}\bullet$  radicals to prevent over-oxidation, significantly improving the selectivity toward nitriles. This amalgamation of function and synergy of the Fe(III)-doped  $\text{TiO}_2$  and  $\text{NH}_4\text{Br}$  reveals new opportunities for developing semiconductor-based photocatalytic systems for fine chemical synthesis.



## INTRODUCTION

Nitriles are important intermediates in organic synthesis and a crucial moiety with a wide application in medicinal, organic, and polymer chemistry.<sup>1,2</sup> General methods for synthesizing nitriles mainly include the nucleophilic cyanation of alkyl halides,<sup>3</sup> Wittig reactions,<sup>4</sup> and transition-metal-catalyzed cyanation of arenes.<sup>5,6</sup> However, these methods demonstrate the drawbacks associated with using high-cost starting materials, the generation of toxic wastes, and the poor atomic efficiency. Therefore, much effort has been devoted to developing novel catalytic methods for the environmentally friendly synthesis of nitriles.

Refining renewable biomass can produce significant quantities of oxygen-containing compounds, such as aldehydes and alcohols, which are versatile raw materials for industries.<sup>7,8</sup> Direct ammoxidation of alcohols and aldehydes into nitriles is an ideal green process as it uses feedstocks from sustainable biomass, and water is the only byproduct.<sup>9–11</sup> The production of nitriles using thermal-catalytic methods has been well documented for the ammoxidation of alcohols and aldehydes using noble-metal catalysts or transition-metal catalysts.<sup>12–14</sup>

Ammoxidation of alcohols to yield nitriles involves the selective oxidation of the alcohol. Most thermal-catalytic systems require high reaction temperatures (to 100 °C) and high-pressure oxygen, which can produce a range of undesirable byproducts. Therefore, conducting ammoxidation under mild conditions has been considered of great importance.<sup>11,14</sup>

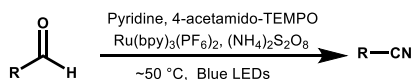
Photocatalytic redox reactions over semiconductors can proceed at room temperature and have received increasing attention in the organic synthetic community.<sup>15,16</sup> The photocatalytic process generates reactive species such as photogenerated charge carriers and oxidative free radicals at room temperature. Developing photocatalytic systems using

Received: July 5, 2022

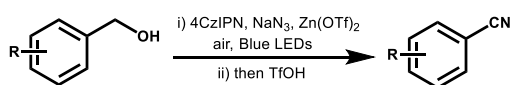
cheap and abundant materials as catalysts is challenging while simultaneously achieving a high reaction rate and product selectivity. This is particularly hard when producing nitriles from alcohols and aldehydes using  $\text{NH}_3$  and  $\text{O}_2$ , as side reactions from overoxidation are hard to avoid.<sup>17–19</sup> Nandi and Leadbeater developed a homogeneous Ru-complex photocatalytic system to synthesize nitriles from aldehydes using  $\text{NH}_4\text{CO}_2\text{NH}_2$  as the nitrogen source, 4-acetamido-TEMPO as the primary oxidant, ammonium persulfate as the secondary oxidant, and pyridine as the base (Scheme 1, reaction A).<sup>18</sup> A

### Scheme 1. Methods Reported in the Literature and the Present Work for the Photocatalytic Ammoxidation of Aldehydes or Alcohols into Nitriles

#### (A) Ammoxidation of aldehydes by $(\text{NH}_4)_2\text{S}_2\text{O}_8$

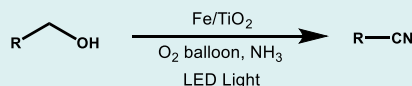


#### (B) Two-step ammoxidation of aromatic alcohols by $\text{NaN}_3$



#### (C) This work:

#### One-pot ammoxidation of aliphatic and aromatic alcohols by $\text{NH}_3$



- 1) Readily available  $\text{NH}_3$  as the nitrogen source
- 2) Low cost of non-noble metal catalyst
- 3) Recyclable heterogeneous catalyst
- 4) High activity and selectivity
- 5) Broad substrate range

relatively simple photocatalytic system utilizing macro-rings was developed for the oxidative transformation of alcohols into nitriles in the presence of Lewis acid. While simple, the reaction required the explosive sodium azide ( $\text{NaN}_3$ ) as the nitrogen source (Scheme 1, reaction B).<sup>19</sup> Obviously, it is highly desirable to develop novel heterogeneous non-noble metal catalytic systems for the photo-ammoxidation of biomass-derived alcohols into nitriles using the low-cost and readily available  $\text{NH}_3$  as the nitrogen source.

$\text{TiO}_2$  is one of the most abundant and extensively studied semiconductors for photochemical applications, such as the degradation of volatile organic compounds, various organic syntheses, and dye-sensitized solar cells.<sup>20–22</sup> Particularly, it is very stable in organic solutions. Thus, its application in photocatalytic organic transformations has greatly attracted research attention. For photocatalytic oxidation reactions,  $\text{TiO}_2$  can generate highly reactive oxygen species such as hydroxylic radicals ( $\cdot\text{OH}$ ), resulting in extensive oxidation and even complete mineralization. However, in the current case, the over-oxidation of reactant alcohols to carboxylic acids would result in poor selectivity and minimal production of the product nitriles. Over-oxidation is a common problem in aerobic oxidation over  $\text{TiO}_2$  photocatalysts, impeding their application for fine chemical synthesis. To achieve high selectivity toward nitriles, we have to design a photocatalytic system that promotes the selective aerobic oxidation of

alcohols to the corresponding aldehydes, which react with ammonia to yield aldimine intermediates ( $\text{RCH}=\text{NH}$ ). The aldimine dehydrogenation by  $\text{O}_2$  yields nitriles. Practical approaches need to be developed to avoid other side reactions. Such procedures would help develop other fine chemical syntheses over Ti-based photocatalysts. It is this idea that motivates us for the present research.

Modifying  $\text{TiO}_2$  with transition metals<sup>23</sup> such as Fe, Mn, and Cu is a facile and effective way to tune the photocatalytic performance of  $\text{TiO}_2$ . Among the transition metals, iron is one of the most appropriate candidates.<sup>24</sup> It can be easily incorporated into the crystal lattice of  $\text{TiO}_2$ , such as in ilmenite, due to the similar radius of  $\text{Fe}^{3+}$  (0.79 Å) and  $\text{Ti}^{4+}$  (0.75 Å).<sup>25</sup> The incorporated iron may improve the separation of  $e^-/h^+$  pairs by capturing electrons, facilitating the formation of active  $\cdot\text{O}_2^-$  radicals.<sup>26</sup>

Another challenge is to find a process to convert the photogenerated holes and  $\text{OH}\cdot$  radicals into milder oxidants that selectively oxidize the reactant alcohols and dehydrogenate the intermediate while avoiding over-oxidation. In the present study, Fe(III)-modified titanium dioxide ( $\text{Fe}/\text{TiO}_2$ ) was prepared by a simple impregnation-calcination method. We found that the  $\text{Fe}/\text{TiO}_2$  catalyst is robust for the ammoxidation of alcohols to nitriles using ammonia as the nitrogen source and  $\text{NH}_4\text{Br}$  as the redox additive (Scheme 1, reaction C).

## RESULTS AND DISCUSSION

Iron-modified  $\text{TiO}_2$  catalysts were prepared by the facile impregnation-calcination method, abbreviated as  $\text{Fe-}x/\text{TiO}_2$  ( $x$  represents the calculated weight percentages of Fe to  $\text{TiO}_2$ , which were set to be 0.3, 1.1, 2.0, and 6.0). X-ray diffraction (XRD) (Figure 1a) was used to investigate the crystal

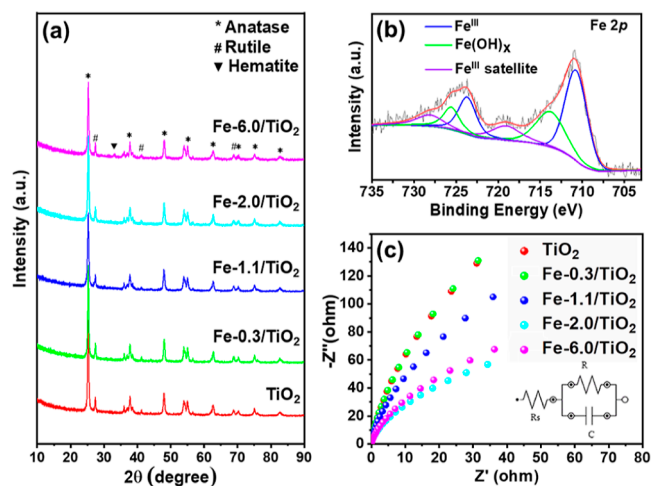


**Figure 1.** (a) XRD patterns of  $\text{TiO}_2$  and  $\text{Fe-}x/\text{TiO}_2$  ( $x = 0.3, 1.1, 2.0,$  and  $6.0$ ), (b) Fe 2p XPS spectrum and corresponding fitted curves of  $\text{Fe-}2.0/\text{TiO}_2$ , and (c) EIS Nyquist spectra of  $\text{TiO}_2$  and  $\text{Fe-}x/\text{TiO}_2$ .

structures of the samples produced.  $\text{Fe-}x/\text{TiO}_2$  composites retained the anatase (PDF#21-1272) and rutile (PDF#21-1276) lattices, while the diffraction patterns associated with iron species were not observed in the as-prepared  $\text{Fe-}x/\text{TiO}_2$  catalysts except for the  $\text{Fe-}6.0/\text{TiO}_2$  sample with the highest iron content. The XRD patterns of  $\text{Fe-}6.0/\text{TiO}_2$  show a weak diffraction peak at  $33^\circ$ , which can be assigned to the hematite

(104) plane (PDF#33-0664), probably because of the crystallization and aggregation of  $\alpha$ -Fe<sub>2</sub>O<sub>3</sub> in the sample.

To figure out the valence states of the iron species, we conducted an X-ray photoelectron spectroscopy (XPS) analysis. The Fe 2p XPS spectrum (Figure 1b) can be fitted into six peaks. Two prominent peaks with binding energies at 710.7 and 723.7 eV are associated with Fe(III) 2p<sub>3/2</sub> and 2p<sub>1/2</sub>, respectively, and are accompanied by two satellite peaks at 719.1 and 728.2 eV. The other two peaks with the binding energies at 713.9 and 725.6 eV are assigned to Fe 2p<sub>3/2</sub> and Fe 2p<sub>1/2</sub> of the Fe-hydroxide groups.<sup>26,27</sup> The peak at 458.7 eV in the Ti 2p spectrum of the Fe-*x*/TiO<sub>2</sub> samples shifts slightly toward a lower binding energy than that of pristine TiO<sub>2</sub> (Figure S1, Supporting Information). This is because Fe species interact with Ti and O on the surface of the TiO<sub>2</sub>, resulting in the lower charge density of the Fe atoms and higher charge density of the Ti atoms, leading to the lower Ti electron binding energy in the XPS spectrum.<sup>24,25</sup>

The transmission electron microscopy (TEM) image (Figure 2a) shows that the morphology of Fe-2.0/TiO<sub>2</sub> was characteristic of nanoparticles with an average size of ~20 nm. No visible iron oxide nanoparticles were observed in the TEM image of Fe-2.0/TiO<sub>2</sub>, consistent with the results of XRD. High-resolution TEM (HR-TEM) was further used to identify the Fe species. As shown in Figure 2b, a lattice fringe with a distance of 0.360 nm was measured in the HR-TEM of Fe-2.0/TiO<sub>2</sub>, which was assigned to the (101) plane of anatase, and was slightly larger than the standard 0.352 nm (PDF#21-1272) for pure TiO<sub>2</sub>. It is consistent with the observation that the characteristic X-ray diffraction peak corresponding to the (101) crystal plane is slightly shifted to a lower angle compared to that of pristine TiO<sub>2</sub> (Figure S2a) because replacing some Ti<sup>4+</sup> by Fe<sup>3+/2+</sup> results in a slight lattice expansion according to the Bragg equation ( $2d\sin\theta = n\lambda$ ). Interestingly, we measured the lattice spacings at different regions and found inconsistent lattice fringe spacing (0.354–0.366 nm) at several places, as shown in Figure S2b. This indicates that the Fe doping is not uniform. Such an enlargement was also noted in the HR-TEM images of the Fe-0.3/TiO<sub>2</sub> sample (Figure S3a–c). In Figure 2c, suspected Fe species are marked by red circles, which shows that the doped Fe species are well dispersed within the TiO<sub>2</sub> lattice. Scanning TEM and the corresponding energy-dispersive X-ray elemental mapping images of Fe-2.0/TiO<sub>2</sub> (Figure 2e–h; Figure S4) further show the distribution of Fe, Ti, and O. Specifically, the spatial distributions of Fe and Ti coincided with each other, which is the general characteristic of doping.<sup>24,29</sup> To investigate the vertical distribution of doped Fe in the TiO<sub>2</sub> lattice, Ar-sputtering XPS measurements at different surface depths were conducted (Figure S4). It is obvious that the iron signal gradually weakens with the sputtering time. When the sputtering time was extended to 1000 s, the iron signal almost completely disappeared, indicating that there are negligible iron species at this depth. The result confirms that the Fe species are located preferentially on the external surface, and with the increase of depth, the content of Fe species gradually declined. These results, combined with the results from XRD patterns, HR-TEM images, and the elemental mapping images, allow us to conclude that the Fe species preferentially existed on the surface of TiO<sub>2</sub>. In an extensive screening of the Fe-2.0/TiO<sub>2</sub> sample in multiple HR-TEM views, the lattice spacing of 0.252 nm corresponding to the (110) plane of hematite (PDF#33-0664) was occasionally observed (Figure 2d). This illustrated

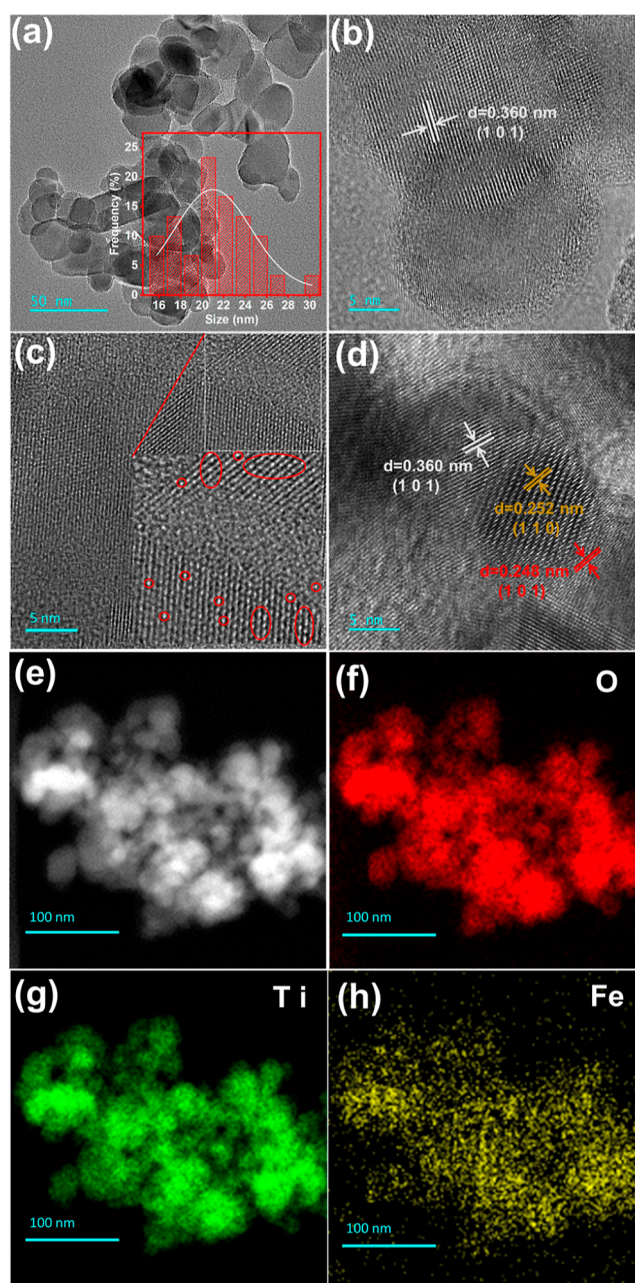


**Figure 2.** (a,b) TEM images (the inset figure is the particle size distribution), (c,d) HRTEM images, and (e–h) elemental mapping of Fe-2.0/TiO<sub>2</sub>.

the formation of small amounts of  $\alpha$ -Fe<sub>2</sub>O<sub>3</sub> highly dispersed within the Fe-2.0/TiO<sub>2</sub> sample. The small quantity and crystallite size explain why the diffraction peaks of  $\alpha$ -Fe<sub>2</sub>O<sub>3</sub> were not detected in XRD. Nevertheless, the lattice fringes of  $\alpha$ -Fe<sub>2</sub>O<sub>3</sub> were not found during the screening of multiple areas of the Fe-0.3/TiO<sub>2</sub> samples (Figure S3a–c). This indicates that the crystallization of  $\alpha$ -Fe<sub>2</sub>O<sub>3</sub> is minimal when the iron content is very low and, instead, Fe(III) is dispersed within the surface lattice of TiO<sub>2</sub>.

To further reveal the fine structure of Fe-2.0/TiO<sub>2</sub>, the X-ray absorption near-edge structure (XANES) and the extended X-ray absorption fine structure (EXAFS) were measured (Figure 3). The spectrum of Fe-2.0/TiO<sub>2</sub> was distinct from the other reference standards in the range of 7120–7160 eV (Figure 3a), suggesting the state of Fe in Fe-2.0/TiO<sub>2</sub> was different from

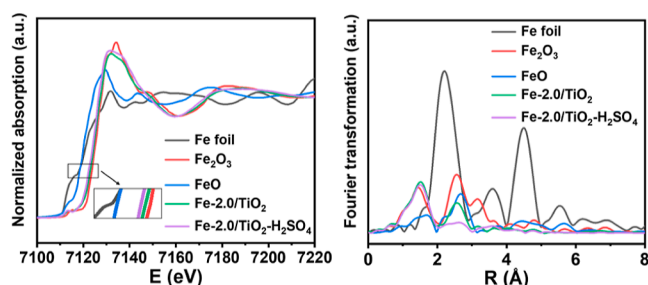


**Figure 3.** (a) Fe K-edge XANES and (b) Fourier transform EXAFS spectra of Fe-2.0/TiO<sub>2</sub>, acid-treated Fe-2.0/TiO<sub>2</sub> (Fe-2.0/TiO<sub>2</sub>-H<sub>2</sub>SO<sub>4</sub>), and reference standards.

that in a standard sample of FeO<sub>x</sub>. These differences are ascribed to the replacement of Fe in the TiO<sub>2</sub> lattice, as it resulted in a different Fe–O bond environment from that in FeO<sub>x</sub>.<sup>30,31</sup> Moreover, the Fe K-edge EXAFS spectrum displays two clear peaks at 1.49 and 2.55 Å, which are assigned to the characteristic peaks of the Fe–O bond and the Fe–O–Fe bond, respectively. No characteristic peak of the Fe–Fe bond at 2.21 Å is observed. The above result demonstrated that iron species existed in both dopants in TiO<sub>2</sub> and iron oxides on the Fe-2.0/TiO<sub>2</sub> surface.

The photocatalytic activities of samples for the ammoxidation of benzyl alcohol are summarized in Table 1. Control experiments revealed that light and O<sub>2</sub>, the essential components for photocatalysis, are required to yield the

**Table 1. Photocatalytic Conversion of Benzyl Alcohol to Benzonitrile<sup>a</sup>**

entry	photocatalyst	conv. 1 (%)	Sel. 2 (%)	Sel. 3 (%)
1	TiO <sub>2</sub>	49.2	4.3	8.7
2	Fe-0.3/TiO <sub>2</sub>	48.4	6.6	19.2
3	Fe-1.1/TiO <sub>2</sub>	47.7	17.8	56.6
4	Fe-2.0/TiO <sub>2</sub>	49.6	17.1	73.8
5	Fe-6.0/TiO <sub>2</sub>	27.4	24.1	66.4
6 <sup>b</sup>	FeCl <sub>3</sub> + TiO <sub>2</sub>	49.5	3.2	13.3
7	FeCl <sub>3</sub>	0	0	0
8 <sup>b</sup>	Fe <sub>2</sub> O <sub>3</sub> + TiO <sub>2</sub>	35.6	63.2	24.3
9	Fe <sub>2</sub> O <sub>3</sub>	0	0	0
10 <sup>c</sup>	Fe-0.3/TiO <sub>2</sub> -H <sub>2</sub> SO <sub>4</sub>	40.7	10.8	24.6
11 <sup>c</sup>	Fe-2.0/TiO <sub>2</sub> -H <sub>2</sub> SO <sub>4</sub>	42.5	22.8	52.9
12 <sup>d</sup>	Fe-2.0/TiO <sub>2</sub>	76.9	1.5	98.5
13 <sup>e</sup>	Fe-2.0/TiO <sub>2</sub>	>99.0	0	>99.0
14 <sup>f</sup>	Fe-2.0/TiO <sub>2</sub>	78.1	89.0	11.0
15 <sup>f</sup>	TiO <sub>2</sub>	>99.0	40.6	1.0
16 <sup>g</sup>	Fe-2.0/TiO <sub>2</sub>	72.8	2.1	91.9

<sup>a</sup>Reaction conditions: benzyl alcohol (0.2 mmol), photocatalyst (20 mg), CH<sub>3</sub>CN (10 mL), 4 Å MS (molecular sieve) (50 mg), NH<sub>3</sub> (0.1 MPa), O<sub>2</sub> balloon, 365 nm LED, 12 h, room temperature. <sup>b</sup>A mechanical mixture of FeCl<sub>3</sub> or Fe<sub>2</sub>O<sub>3</sub> and TiO<sub>2</sub>; the iron content was the same as that in Fe-2.0/TiO<sub>2</sub>. <sup>c</sup>Fe/TiO<sub>2</sub>-H<sub>2</sub>SO<sub>4</sub> represents that the catalyst was washed with 0.5 M sulfuric acid for 12 h before use. <sup>d</sup>H<sub>4</sub>Br (0.25 equiv). <sup>e</sup>NH<sub>4</sub>Br (0.25 equiv), 24 h. <sup>f</sup>NH<sub>4</sub>Br (0.25 equiv) without NH<sub>3</sub>. <sup>g</sup>NH<sub>4</sub>Br (0.25 equiv) and water (0.1 mL) without 4 Å MS.

desired product (Table S1). Pristine TiO<sub>2</sub>, the Fe-*x*/TiO<sub>2</sub> catalysts (except for Fe-6.0/TiO<sub>2</sub>), and a mechanical mixture of FeCl<sub>3</sub> or Fe<sub>2</sub>O<sub>3</sub> and TiO<sub>2</sub> (Table 1, entries 6 and 8) showed similar conversions of benzyl alcohol, while FeCl<sub>3</sub> and Fe<sub>2</sub>O<sub>3</sub> exhibited no catalytic activity toward the conversion (Table 1, entries 7 and 9). The alcohol reactant is first oxidized to the corresponding aldehyde, followed by a cyanation of the aldehyde with ammonia to yield a nitrile product.<sup>10,12</sup> Thus, the above results reveal that the illuminated TiO<sub>2</sub> is necessary for generating oxidative species for the aerobic oxidation of alcohol reactants. However, most benzyl alcohols were converted into over-oxidized products on pure TiO<sub>2</sub>, such as benzoic acid and benzyl benzoate (Figure S5), which are not reactive for the subsequent cyanation with ammonia (Table S2, entry 5). The selectivities for benzaldehyde and benzonitrile over TiO<sub>2</sub> are only 8.7 and 4.3% (Table 1, entry 1), respectively.

**Effect of Fe(III) Modification.** The results in Table 1 show that as the Fe loading increases from 0.3 to 2.0% (entries 2–4), the selectivity to benzaldehyde and benzonitrile increases considerably, while the alcohol conversion varies slightly. In this iron content range, more dispersed Fe(III) species are in the TiO<sub>2</sub> lattice, coinciding with less alcohol being over-oxidized. The Fe(III) species in the TiO<sub>2</sub> lattice reduces the over-oxidation to benzoic acid and benzyl benzoate, contributing to the formation of benzonitrile. Fe-2.0/TiO<sub>2</sub> delivered the highest selectivity of benzonitrile at 73.8%, while the selectivity of benzaldehyde was 17.1% (Table 1, entry 4). Comparing entries 4 and 5 in Table 1, one can see that the dispersed Fe(III) species also promote benzaldehyde cyanation. In addition, The diffuse reflectance UV–VIS spectra of the Fe-*x*/TiO<sub>2</sub> samples show a red shift in the visible region compared to those of the pristine TiO<sub>2</sub> (Figures S6a,b). Increasing the Fe loading to 6.0% caused a color change in the samples, from light yellow to dark yellow and finally to brown.

Further increasing the Fe loading from 2.0 to 6.0%, the conversion of benzyl alcohol decreased from 49.6% over Fe-2.0/TiO<sub>2</sub> to 27.4% over Fe-6.0/TiO<sub>2</sub> (Table 1, entry 5). The electrochemical impedance spectroscopy (EIS) Nyquist spectra in Figure 1c show that the increase of the Fe loading to 6.0% causes a decrease in the transfer efficiency of light-generated charge carriers. The lower transfer efficiency generates fewer reactive species for oxidation and affects the benzyl alcohol oxidation. The mechanical mixture of FeCl<sub>3</sub> and TiO<sub>2</sub> exhibited poor selectivity for benzonitrile. The Fe<sup>3+</sup> species bonded to the TiO<sub>2</sub> surface are responsible for the slight increase in the benzonitrile selectivity compared with that on the pure TiO<sub>2</sub> catalyst.

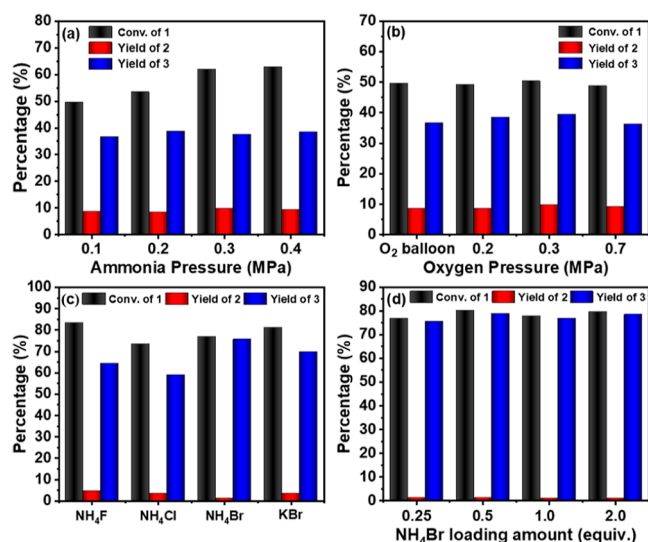
The modification of TiO<sub>2</sub> with Fe(III) significantly improved the yields of benzonitrile but not the benzyl alcohol conversion, indicating that Fe(III) enhanced the cyanation of benzaldehyde with ammonia to yield benzonitrile, as evidenced by the control experiments shown in Table S2. We conducted the control experiments over Fe-2.0/CeO<sub>2</sub>, Fe-2.0/CdS, and Fe-2.0/BiVO<sub>4</sub> to investigate which step in the ammoxidation reactions is responsible for the poor performance compared to Fe-2.0/TiO<sub>2</sub>. The result in Table S3 reveals that when exposed to the NH<sub>3</sub> atmosphere, Fe-2.0/CeO<sub>2</sub>, Fe-2.0/CdS, and Fe-2.0/BiVO<sub>4</sub> lost the ability to photocatalytically activate benzyl alcohol oxidation. Since Fe(III) existed both as a lattice dopant and as α-Fe<sub>2</sub>O<sub>3</sub> in Fe-2.0/TiO<sub>2</sub>, to clarify the role of the tiny α-Fe<sub>2</sub>O<sub>3</sub> supported on the TiO<sub>2</sub> surface, we used 200 mg of catalysts and 40 mL of 0.5 M sulfuric acid to reflux at 70 °C for

12 h to remove  $\alpha$ -Fe<sub>2</sub>O<sub>3</sub> while retaining the doped iron. Further, we conducted two supplemental reactions over Fe-0.3/TiO<sub>2</sub>-H<sub>2</sub>SO<sub>4</sub> and Fe-2.0/TiO<sub>2</sub>-H<sub>2</sub>SO<sub>4</sub> catalysts, which were characterized by TEM (Figures S3 and S7).

We noted that the benzonitrile yields over Fe-0.3/TiO<sub>2</sub> and Fe-0.3/TiO<sub>2</sub>-H<sub>2</sub>SO<sub>4</sub> are similar (Table 1, entries 2 vs 10), while the benzonitrile yield decreased substantially from 36.6% over Fe-2.0/TiO<sub>2</sub> to 22.5% over Fe-2.0/TiO<sub>2</sub>-H<sub>2</sub>SO<sub>4</sub> (Table 1, entries 4 vs 11). As shown in Figure 3, Fe-2.0/TiO<sub>2</sub>-H<sub>2</sub>SO<sub>4</sub>, Fe-2.0/TiO<sub>2</sub>, and the standard samples show pre-edge peaks at 7115–7125 eV. The pre-edge peaks of the two catalysts are located between the peaks of FeO and Fe<sub>2</sub>O<sub>3</sub>. In comparison, the peak of Fe-2.0/TiO<sub>2</sub>-H<sub>2</sub>SO<sub>4</sub> shows a little negative shift compared to that of Fe-2.0/TiO<sub>2</sub>. It implies that the oxidation state of Fe in the two catalysts is between +2 and +3, and the oxidation state of Fe in Fe-2.0/TiO<sub>2</sub>-H<sub>2</sub>SO<sub>4</sub> is lower than that in Fe-2.0/TiO<sub>2</sub>. This is because the oxygen coordination number of Fe-2.0/TiO<sub>2</sub>-H<sub>2</sub>SO<sub>4</sub> ( $5.7 \pm 0.3$ ) is less than that of Fe-2.0/TiO<sub>2</sub> ( $6.0 \pm 0.2$ ) (Table S4) so that the oxidation state of Fe over Fe-2.0/TiO<sub>2</sub>-H<sub>2</sub>SO<sub>4</sub> is lower.<sup>30,31</sup>

Moreover, the iron oxide particles on the catalyst surface were removed after acid treatment. Therefore, the characteristic peak of the Fe–O–Fe bond at 2.55 Å is not observed in the EXAFS spectrum of Fe-2.0/TiO<sub>2</sub>-H<sub>2</sub>SO<sub>4</sub> (Figure 3b). This means that iron is doped on the Fe-2.0/TiO<sub>2</sub>-H<sub>2</sub>SO<sub>4</sub> surface on an atomic scale.<sup>30</sup> The reduced yield of benzonitrile after the acid treatment of Fe-2.0/TiO<sub>2</sub> reveals that both Fe(III) dopants and  $\alpha$ -Fe<sub>2</sub>O<sub>3</sub> are active in photocatalytic ammoxidation. Similar yields of benzonitrile from Fe-0.3/TiO<sub>2</sub> and Fe-0.3/TiO<sub>2</sub>-H<sub>2</sub>SO<sub>4</sub> further confirm that Fe species were present in the dopant states at low loading (e.g., 0.3%), which was consistent with the results shown in the characterization section. We further ruled out the activity of  $\alpha$ -Fe<sub>2</sub>O<sub>3</sub>, and the reaction was inactive when the catalyst was replaced with  $\alpha$ -Fe<sub>2</sub>O<sub>3</sub> and  $\alpha$ -Fe<sub>2</sub>O<sub>3</sub> was mechanically mixed with TiO<sub>2</sub> (Table 1, entries 8 and 9).

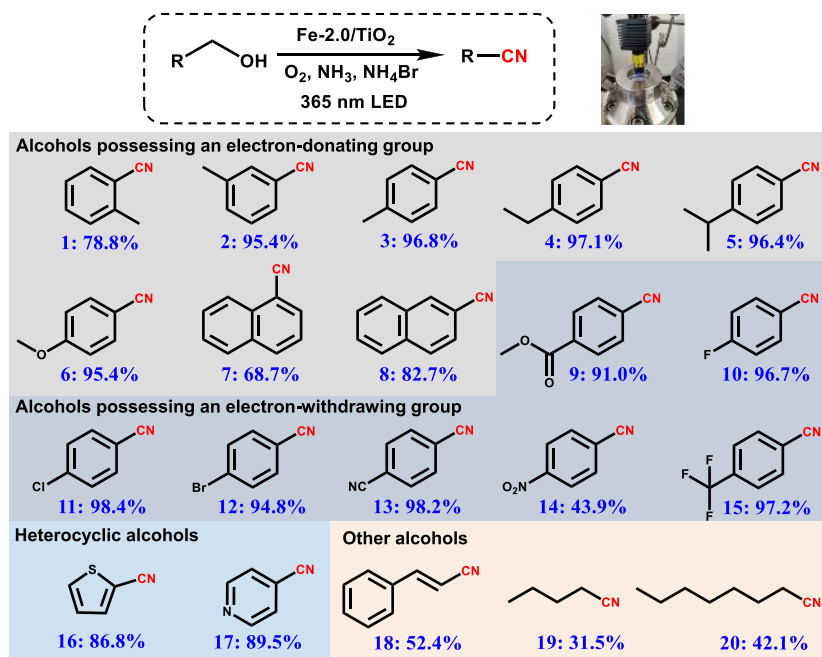
Moreover, NH<sub>3</sub> temperature-programmed desorption (NH<sub>3</sub>-TPD) profiles showed that the strong acid sites with the desorption peak of NH<sub>3</sub> at 390 °C were significantly enhanced after introducing Fe species to the TiO<sub>2</sub> (Figure 5a). This means that the Fe(III) modification increases the adsorption of NH<sub>3</sub> on the catalyst. The adsorption of the intermediates with an amino group, such as RCH=NH, should be enhanced because the interaction between the amino group and the surface is enhanced. The enhanced adsorption accelerates their reactions toward yielding nitriles. We observed a substantial decrease in nitrile yield when adding pyridine (which blocks the surface sites for the adsorption of NH<sub>3</sub> and the intermediates). This indicates that the catalyst surface sites play an essential role in aldehyde cyanation with NH<sub>3</sub>. Fe (III) dopants improved the surface properties, promoting cyanation (reaction 4 vs reaction 6, Scheme 3a). The above results confirm that an exquisite modification of TiO<sub>2</sub> with Fe(III) can serve to control the reaction pathway, improving the selectivity of benzonitrile. The reaction conditions were then optimized over Fe-2.0/TiO<sub>2</sub>. In our experimental procedure, NH<sub>3</sub> was first filled before O<sub>2</sub> was charged into the autoclave. As shown in Figure 4a, the pressure of NH<sub>3</sub> gas influenced the reaction. 0.1 MPa of NH<sub>3</sub> gave the highest selectivity of the product, while excessive NH<sub>3</sub> decreased the benzonitrile selectivity. The pressure of oxygen has a negligible influence on the benzonitrile yield (Figure 4b). Thus, an oxygen balloon was used to provide sufficient O<sub>2</sub>.



**Figure 4.** Optimization of oxygen pressure, ammonia pressure, species of HAT, and NH<sub>4</sub>Br loading amount. Reaction conditions: benzyl alcohol (0.2 mmol), the Fe-2.0/TiO<sub>2</sub> catalyst (20 mg), CH<sub>3</sub>CN (10 mL), 4Å MS (50 mg), 365 nm LED, room temperature, 12 h, except for the (a) O<sub>2</sub> balloon without the HAT agent, (b) NH<sub>3</sub> (0.1 MPa) without the HAT agent, (c) 1.0 equiv of the HAT agent, the O<sub>2</sub> balloon, and NH<sub>3</sub> (0.1 MPa), and (d) NH<sub>4</sub>Br, the O<sub>2</sub> balloon, and NH<sub>3</sub> (0.1 MPa).

**Effect of the NH<sub>4</sub>Br Additive.** Excellent benzonitrile yield was achieved by adding NH<sub>4</sub>Br to the reaction mixture (Table 1, entries 12 and 13). NH<sub>4</sub>Br likely promotes photocatalytic ammoxidation *via* a combination of two effects. Halogen anions can serve as the hydrogen atom transfer (HAT) agents in radical reactions, mediating and accelerating the photocatalytic reactions.<sup>32,33</sup> As shown in Figure 4c, adding HAT agents, NH<sub>4</sub>F, NH<sub>4</sub>Cl, NH<sub>4</sub>Br, and KBr, positively affected the photocatalytic ammoxidation of benzyl alcohol. The benzonitrile yield in the presence of KBr is higher than those with NH<sub>4</sub>F or NH<sub>4</sub>Cl. This means that Br<sup>-</sup> anions contributed more to improving the catalytic efficiency. Br<sup>-</sup> ions reacted with positively charged holes, yielding Br<sup>•</sup> radicals that increase the alcohol conversion while avoiding over-oxidation. NH<sub>4</sub>Br is the best additive also because NH<sub>4</sub><sup>+</sup> in NH<sub>4</sub>Br may serve as the nitrogen source for the formation of benzonitrile, as shown in the reaction without NH<sub>3</sub> (Table 1, entry 14). A similar reaction was conducted with pure TiO<sub>2</sub> (Table 1, entry 15). The result also demonstrates that alcohol is more prone to over-oxidation without iron modification. 0.25 equiv of NH<sub>4</sub>Br gave the best nitrile yield. Increasing the loading past this point, NH<sub>4</sub>Br does not increase the nitrile yield (Figure 4d), possibly due to the poor solubility of NH<sub>4</sub>Br in acetonitrile (Figure S8). We also investigated the influence of NH<sub>3</sub> by control experiments with/without NH<sub>3</sub> in the presence of HAT. Table S5 shows that the yield of benzaldehyde changed from trace to 7.3%, the yield of overoxidation products (benzoic acid and benzyl benzoate) increased from negligible to 79.0%, and the yield of nitrile decreased from 99.0 to 9.3%. These results indicate that the presence of NH<sub>3</sub> restrains the overoxidation of benzyl alcohol.

Adding water to the reaction system inhibited the reaction to a certain extent (Table 1, entry 16). Thus, adding molecular sieves is required to remove water formed during the reaction. Under the optimal conditions, the benzonitrile yield was 99.0%

Scheme 2. Substrate Scope for the Photocatalytic Ammoxidation of Alcohols into Nitriles<sup>a</sup>

<sup>a</sup>Reaction conditions: substrate (0.2 mmol), Fe-2.0/TiO<sub>2</sub> (20 mg), CH<sub>3</sub>CN (10 mL), 4 Å MS (50 mg), NH<sub>3</sub> (0.1 MPa), NH<sub>4</sub>Br (0.25 equiv), O<sub>2</sub> balloon, 365 nm LED, room temperature, and 24 h.

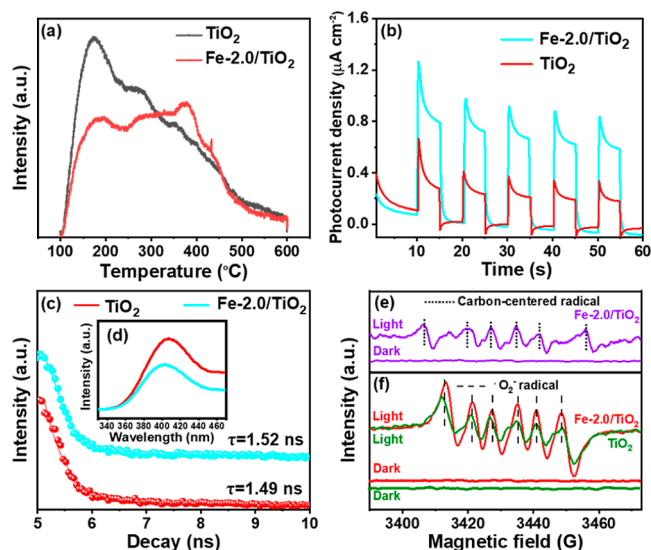
within 24 h (Table 1, entry 13). Surprisingly, this system also obtained an 80.3% yield under sunlight irradiation (Figure S9).

Besides the high catalytic activity and the excellent selectivity toward benzonitrile, the Fe-2.0/TiO<sub>2</sub> catalyst also demonstrated high stability after five cycles without a noticeable loss of activity and no significant changes of the initial oxidation rates and the temporal profile of product formation (Figure S10). The recycled catalyst was characterized by XRD, TEM, XPS, ICP-AES, and so on (Figures S11–13 and Table S6). The results were not significantly different from those before use, indicating that the catalyst was very stable.

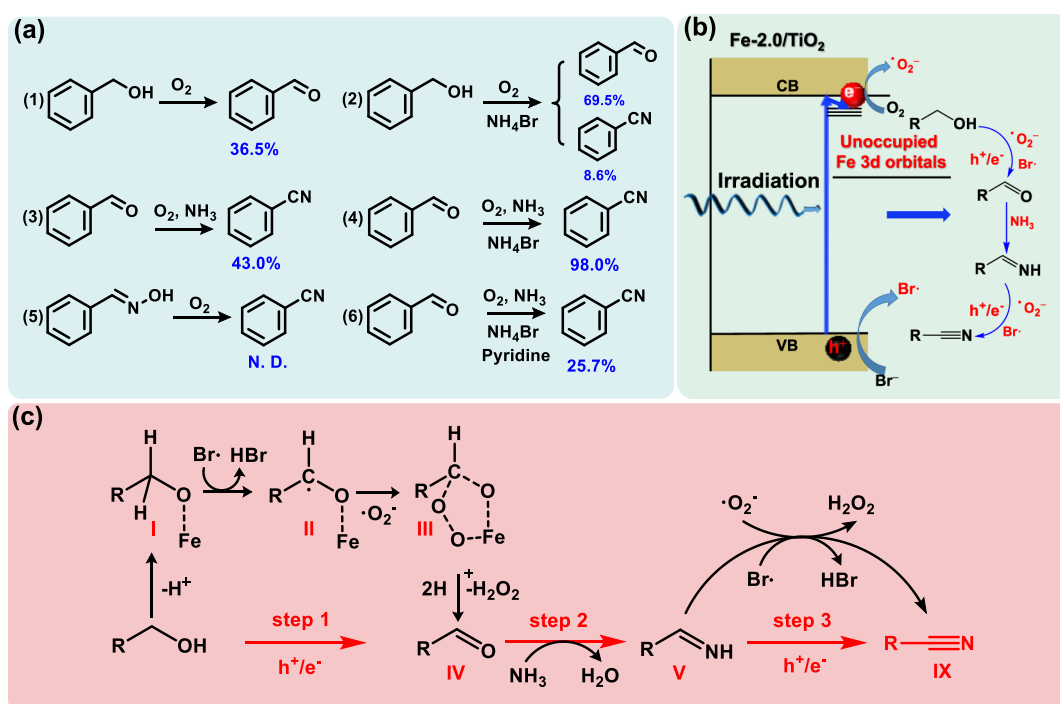
With the optimal reaction conditions in hand, we explored the substrate scope for the photocatalytic ammoxidation of alcohols into nitriles over the Fe-2.0/TiO<sub>2</sub> catalyst (Scheme 2). In general, aromatic and heteroaromatic alcohols were converted into the corresponding nitriles with good to excellent yields. An obvious steric hindrance was observed for the *O*-methyl benzyl alcohol compared to that for *m/p*-methyl benzyl alcohol (products 1 vs 2 and 3). In addition, the electronic properties of the substituent groups, whether electron-donating or -withdrawing, show no significant influence on substrate conversion due to the reaction involving the radicals. The electronic properties generally affect the activity of the substrates involving cation or anion intermediates.<sup>34</sup> A lower yield is observed for product 14 with a nitro group, possibly due to the competitive adsorption of the nitro group with the hydroxyl group on the catalyst surface, thereby reducing the reaction rate.<sup>35,36</sup> Functional groups such as alkyl, ether, ester, halogens, and nitro are well tolerated in our photocatalytic system. 4-Cyanopyridine (17), an important intermediate in synthesizing pharmaceuticals such as Milverin and Pyrazidil, was obtained with a yield of 89.5%. More excitingly, the method developed in the paper is also effective for inert aliphatic alcohols, affording the synthesis of aliphatic nitriles with moderate yields in the same reaction

time. This is challenging when using a thermal-catalytic process.

**Mechanism Study.** Modifying TiO<sub>2</sub> with the Fe(III) species affected the separation and transfer of photogenerated carriers. Under irradiation, the photocurrent density of Fe-2.0/TiO<sub>2</sub> is considerably higher than that of TiO<sub>2</sub> (Figure 5b), indicating that there are more photogenerated electrons over Fe-2.0/TiO<sub>2</sub> than over TiO<sub>2</sub>. The EIS Nyquist spectra also



**Figure 5.** (a) NH<sub>3</sub>-TPD profile of Fe-2.0/TiO<sub>2</sub> and TiO<sub>2</sub>, (b) photocurrent densities of TiO<sub>2</sub> and Fe-2.0/TiO<sub>2</sub>, (c) time-dependent photoluminescence lifetime spectra of TiO<sub>2</sub> and Fe-2.0/TiO<sub>2</sub>, (d) room temperature photoluminescence emission spectra of TiO<sub>2</sub> and Fe-2.0/TiO<sub>2</sub>, electron paramagnetic resonance spectra of (e) carbon-centered radical (<sup>•</sup>C) and (f) superoxide radical (<sup>•</sup>O<sub>2</sub><sup>-</sup>) using 5,5-dimethyl-1-pyrroline *N*-oxide as a spin-trapping agent.

Scheme 3. (a) Control Experiments; (b) Scheme of the Generation of Active Radicals; and (c) Proposed Three-Step Reaction Mechanism<sup>a</sup>

<sup>a</sup>General conditions: substrate (0.2 mmol), Fe-2.0/TiO<sub>2</sub> (20 mg), CH<sub>3</sub>CN (10 mL), 4 Å MS (molecular sieve) (50 mg), 365 nm LED, 12 h, room temperature.

indicate that the separation and transfer of charge carriers are enhanced by Fe(III) doping (Figure 1c). The photoluminescence spectra show that the Fe-2.0/TiO<sub>2</sub> sample exhibits a lower fluorescence intensity than TiO<sub>2</sub> (Figure 5d). One can deduce that more light-excited electrons were captured by O<sub>2</sub> adsorbed onto Fe-2.0/TiO<sub>2</sub>, yielding more •O<sub>2</sub><sup>-</sup> radicals than pristine TiO<sub>2</sub>. This means fewer electrons relaxed to the valence band with emission, and a lower emission intensity was observed from Fe-2.0/TiO<sub>2</sub> than from pure TiO<sub>2</sub>. Time-resolved photoluminescence was also conducted to detect the exciton lifetime (Figure 5c). The exciton lifetime was 1.49 ns for TiO<sub>2</sub>, which increased to 1.52 ns for Fe-2.0/TiO<sub>2</sub>. These results confirm that the Fe(III) lattice dopants enhanced the separation of photogenerated electron–hole pairs. This increased separation increases the likelihood that reactive species will be produced by the exciton pair, improving the photocatalytic efficiency.<sup>37</sup>

Radical quenching experiments investigated the reactive species produced in the photocatalytic process. Triethanolamine, butylated hydroxytoluene, isopropyl alcohol (IPA), *p*-benzoquinone, and potassium peroxodisulfate (K<sub>2</sub>S<sub>2</sub>O<sub>8</sub>) were used as scavengers for the photogenerated hole (h<sup>+</sup>), carbon-centered radical (•C), hydroxyl radical (•OH), superoxide radical (•O<sub>2</sub><sup>-</sup>), and photoexcited electron (e<sup>-</sup>), respectively. As shown in Figure S14, the activity of aerobic oxidation of benzyl alcohol over Fe-2.0/TiO<sub>2</sub> significantly decreased when the scavengers for h<sup>+</sup>, •C, •O<sub>2</sub><sup>-</sup>, and e<sup>-</sup> were added to the reaction system. This demonstrates that these reactive species played a vital role in this synthesis. Similar quenching results were observed using the intermediate benzaldehyde as the starting material (Figure S15). These radicals promote both the conversion of benzyl alcohol and the cyanation of the intermediate benzaldehyde.

Electron paramagnetic resonance measurements with Fe-2.0/TiO<sub>2</sub> and pristine TiO<sub>2</sub> were conducted using 5,5-dimethyl-1-pyrroline *N*-oxide as the trapping agent. These experiments proved the influence of Fe(III) doping on the generation of two reactive radicals, carbon-centered radicals and •O<sub>2</sub><sup>-</sup> species. As shown in Figure 5e,f, the purple and red plots with two different sextuplet peaks reveal the existence of carbon-centered radicals and •O<sub>2</sub><sup>-</sup> species, respectively.<sup>38,39</sup> The intensity of the •O<sub>2</sub><sup>-</sup> peaks in the Fe-2.0/TiO<sub>2</sub> system is more potent than in pristine TiO<sub>2</sub> under the same conditions (Figure 5f), indicating that more •O<sub>2</sub><sup>-</sup> species were generated over Fe-2.0/TiO<sub>2</sub> than over pure TiO<sub>2</sub>. Thus, these results suggest that more light-excited electrons were captured by the adsorbed O<sub>2</sub> and more carbon-centered radicals were generated on Fe-2.0/TiO<sub>2</sub> than on TiO<sub>2</sub>.

The mechanism for how NH<sub>4</sub>Br contributes to the photocatalytic activity is of great interest as it promotes both the alcohol oxidation and subsequent aldehyde cyanation (Table 1). It has been known that HBr and CH<sub>2</sub>Br<sub>2</sub> could generate Br• through the oxidation of Br<sup>-</sup> by the Mes-Acr<sup>+</sup>ClO<sub>4</sub><sup>-</sup> ( $E_{1/2}(\text{cat}^*/\text{cat}^+) = +2.06 \text{ V vs SCE}$ ) photo-redox catalyst because it has sufficient power for the oxidation of CH<sub>2</sub>Br<sub>2</sub> ( $E_{1/2}^{\text{ox}} = +1.62 \text{ V vs SCE}$ ) and HBr ( $E_{1/2}^{\text{ox}} = +0.76 \text{ V vs SCE}$ ).<sup>32</sup> We have inferred that NH<sub>4</sub>Br improves the photocatalytic efficiency of the transformation of Br<sup>-</sup> to bromide radicals (Br•) during the photocatalytic process. To verify the possibility that Br• radicals exist, we measured the cyclic voltammetry of NH<sub>4</sub>Br (Figure S16). The result indicated that the illuminated Fe-2.0/TiO<sub>2</sub> ( $E_{\text{CB}} = +2.60 \text{ V vs NHE}$ ) could oxidize NH<sub>4</sub>Br ( $E_{1/2}^{\text{ox}} = +1.30 \text{ V vs NHE}$ ) to yield Br• radicals. The generation of Br• from Br<sup>-</sup> over a TiO<sub>2</sub> photocatalyst has been previously reported.<sup>40,41</sup> To prove the existence of Br• radicals in the system, we carried out laser

flash photolysis (LFP) measurements. The direct detection of  $\text{Br}^\bullet$  by LFP was rarely reported, and the detection of  $\text{Br}_2^{\bullet-}$  is usually introduced to identify the presence of  $\text{Br}^\bullet$  ( $\text{Br}^\bullet + \text{Br}^- \rightarrow \text{Br}_2^{\bullet-}$ ). As shown in Figure S17, the generation of  $\text{Br}^\bullet$  is confirmed by the similar absorption peak around 360 nm, which is ascribed to the absorption of  $\text{Br}_2^{\bullet-}$ .<sup>42–44</sup> In addition, we conducted a control experiment with identical photo-reaction conditions, except that phenol was used as the substrate instead of benzyl alcohol and without  $\text{NH}_3$ . As indicated by the GC chromatogram of the products (Figure S18a), 4-bromophenol was the sole product (Figure S18b). Despite its low yield due to the low solubility of  $\text{NH}_4\text{Br}$ , these results reveal the existence of  $\text{Br}^\bullet$  during the photocatalytic reaction as the reaction between phenol and  $\text{Br}^\bullet$  is a well-recognized radical substitution process.<sup>42</sup> Therefore, as shown in Scheme 3b, we deduce that light irradiation excites the valence band electrons to the conduction band, and  $\text{O}_2$  captures the excited electrons to produce  $^{\bullet}\text{O}_2^-$ . The holes in the conduction band of Fe-2.0/ $\text{TiO}_2$  (with potential  $E = +2.60$  V vs NHE) have sufficient power to oxidize  $\text{Br}^-$  anions to generate  $\text{Br}^\bullet$  radicals. This process consumes the most oxidative specie, the photogenerated holes, reducing over-oxidation significantly.

Based on the above analysis and previous reports, we propose a mechanism for the photocatalytic ammoxidation of alcohols into nitriles over the Fe- $x$ / $\text{TiO}_2$  catalyst (Scheme 3c). Aldehydes were detected to be the intermediate in systems with Fe/ $\text{TiO}_2$  photocatalysts (Figure S19).  $\text{NH}_4\text{Br}$  played a dual role: promoting the oxidation of benzyl alcohol to benzaldehyde (reaction 1 vs 2, Scheme 3a) and the subsequent ammoxidation of the benzaldehyde into benzonitrile (reaction 3 vs 4, Scheme 3a). In addition, it can serve as an additional nitrogen source for the ammoxidation of benzaldehyde (reaction 1 vs 2, Scheme 3a).

A recent report on benzaldehyde ammoxidation using  $\text{NH}_2\text{OH}\cdot\text{HCl}$  as the nitrogen source indicated that benzaldoxime was the intermediate in the process,<sup>45</sup> which was formed by the condensation of benzaldehyde and  $\text{NH}_2\text{OH}$ . Interestingly, Fe-2.0/ $\text{TiO}_2$  was inactive in an experiment using benzaldoxime as the substrate (reaction 5, Scheme 3a). Thus, the aldimine intermediate ( $\text{RCH}=\text{NH}$ ) yielded from the condensation of aldehydes with  $\text{NH}_3$  is likely the intermediate in our catalytic system, similar to that reported for thermal and photocatalytic systems.<sup>12,46,47</sup> To demonstrate the existence of imine intermediates, we increased the pressure of  $\text{NH}_3$  to promote the conversion of step 2 (Scheme 3c) to accumulate more product V. The accumulated product V will not only be oxidized to nitrile by dehydrogenation but also spontaneously be condensed to an imine condensate (Figure S20a). The retention time of the condensate in the GC chromatograph was about 17 min (Figure S20b). By analyzing the MS spectrum of the condensate, the structural formula of the product was acquired as 1-phenyl- $N,N'$ -bis(phenylmethylene) (Figure S20c), which was consistent with the previous report.<sup>48</sup> This result also demonstrates the existence of intermediate imines, supporting our proposed mechanism for the oxidation of imines to nitriles. Therefore, the photocatalytic transformation of alcohols into nitriles involves the selective oxidation of alcohols into aldehydes as the first step, followed by condensing the aldehydes with  $\text{NH}_3$  into an aldimine intermediate ( $\text{RCH}=\text{NH}$ ) and the final oxidation of  $\text{RCH}=\text{NH}$  into the nitrile. In these two oxidation steps, the rate of aldehyde ammoxidation to nitrile was slower

in the initial stage of the reaction, and  $\text{NH}_4\text{Br}$  promoted the reaction rates of both steps. It suggested that the process of aldehyde ammoxidation to nitrile was the rate-determining step (Figure S21), similar to the nitrile catalyzed by a palladium catalyst under light irradiation.<sup>13</sup>

Under light irradiation, reactive  $^{\bullet}\text{O}_2^-$  and  $\text{Br}^\bullet$  radicals were generated in this photocatalytic system. The oxidation of alcohols to aldehydes is a selective oxidation reaction, and reaction mechanisms involving  $^{\bullet}\text{O}_2^-$  as the reactive oxygen species have been well documented.<sup>35,36,49,50</sup> Control experiments showed that  $\text{NH}_4\text{Br}$  significantly promoted the oxidation of benzyl alcohol to benzaldehyde in the absence of  $\text{NH}_3$  (reaction 2, Scheme 3a). Thus, it is concluded that the *in situ* formed  $\text{Br}^\bullet$  radicals promoted the generation of the carbon-centered radicals (II) via the cleavage of the  $\text{C}_\alpha\text{--H}$  bond, a critical step in the photocatalytic oxidation of alcohols into aldehydes.<sup>39,49</sup> As excellent HAT agents, bromine anions have been successfully applied in photo-redox catalysis.<sup>32,45,51,52</sup> For example, the selective alkylation and amination of inactive  $\text{C}(\text{sp}^3)\text{--H}$  bonds over a photo-redox catalyst with  $\text{HBr}$  as the HAT agent was reported, in which the *in situ* generated  $\text{Br}^\bullet$  is responsible for the abstraction of the hydrogen atom from the  $\text{C}(\text{sp}^3)\text{--H}$  partner to produce a tertiary radical instead of bromine substitution.<sup>32</sup> It is consistent with our experimental result that no bromine-substituted products were detected. After the generation of the carbon-centered radical (II), the carbon-centered radical (II) couples with  $^{\bullet}\text{O}_2^-$  to generate the Fe-coordinated intermediate (III),<sup>49</sup> followed by the concerted bond-cleavage process to yield the aldehyde intermediate (IV) and the release of  $\text{H}_2\text{O}_2$ .  $\text{H}_2\text{O}_2$  was immediately decomposed on iron species by a Fenton reaction which generates hydroxyl radicals ( $\text{OH}^\bullet$ ) that could over-oxidize benzyl alcohol.<sup>50,53</sup> By introducing  $\text{Br}^-$  into the system, the  $\text{OH}^\bullet$  are preferentially quenched by  $\text{Br}^-$  to generate  $\text{Br}^\bullet$  radicals.<sup>54</sup> To further understand the main role of bromine, we carried out a control experiment with the addition of IPA as a scavenger of hydroxyl radicals in the presence and absence of  $\text{NH}_4\text{Br}$ . The results show that the yield of nitrile slightly decreased after quenching the hydroxyl radical (Table S7). This indicates that quenching hydroxyl radicals have a limited impact on the conversion of both benzyl alcohol and benzaldehyde. The  $\text{Br}^\bullet$  radicals significantly increase the selective oxidation of the alcohol to yield aldehyde but avoid the over-oxidation of benzyl alcohol and promote the ammoxidation of benzyl alcohol to nitrile. The presence of  $\text{NH}_3$  also contributes to the high selectivity of nitrile. In the absence of  $\text{NH}_3$ , over-oxidation products were detected after adding different HAT reagents (Table S5). When benzyl alcohol was oxidized to benzaldehyde, it immediately reacted with ammonia to form imines ( $\text{RCH}=\text{NH}$ , V) (Scheme 3c), a common spontaneous process at room temperature. The imine was further dehydrogenated by aerobic oxidation to yield the final nitrile product rather than being directly oxidized to benzoic acid. To support the proposed mechanism further, we conducted control experiments with toluene as the substrate under identical conditions. As shown in Scheme S1, in the presence of  $\text{NH}_4\text{Br}$ , toluene could be converted to benzaldehyde and benzonitrile. Although the conversion was only 10% due to the inert nature of  $\text{C--H}$  bonds in toluene, we can deduce that  $\text{Br}^\bullet$  indeed contributed to the activation of  $\text{C--H}$  bond dissociation. This result supports our proposed mechanism that  $\text{Br}^\bullet$  contributes greatly to activating  $\text{C--H}$  bonds in benzyl alcohol.



In our photoreaction system, benzyl alcohol is selectively oxidized to benzaldehyde under light conditions (step 1, Scheme 3c), and the aldehyde, immediately spontaneously condenses with  $\text{NH}_3$  to generate an unstable aldimine intermediate ( $\text{RCH}=\text{NH}$ , V) (step 2, Scheme 3c). As previously reported,<sup>12,13,55,56</sup> the aldimine intermediate further oxidatively dehydrates to yield benzonitrile (step 3, Scheme 3c). The synergistic effect of  $\cdot\text{O}_2^-$  radicals and  $\text{Br}\cdot$  radicals greatly promotes steps 1 and 3.

## CONCLUSIONS

We developed a green system composed of a  $\text{Fe}/\text{TiO}_2$  photocatalyst and  $\text{NH}_4\text{Br}$  for catalyzing the ammoxidation of alcohols to produce nitriles using  $\text{O}_2$  and  $\text{NH}_3$  at room temperature, with excellent nitrile yield. The new mechanism found in this study has implications for designing other photocatalytic systems to produce fine chemicals using catalysts and additives from abundant materials. Well-dispersed  $\text{Fe(III)}$  species within a  $\text{TiO}_2$  lattice do not reduce the oxidation potential toward alcohols but effectively enhance the adsorption of  $\text{NH}_3$  and the intermediates and promote the cyanation of the aldehyde intermediates. The  $\text{Br}^-$  ions of the  $\text{NH}_4\text{Br}$  additive are oxidized, yielding reactive  $\text{Br}\cdot$  radicals under light irradiation. These consume powerful oxidants generated in the photocatalytic system, avoiding over-oxidation of the alcohol and increasing the adsorption of  $\text{NH}_3$  and the intermediates. The  $\text{Br}\cdot$  radicals accelerate the cleavage of the  $\text{C}_\alpha\text{-H}$  bond, the critical step involved in the ammoxidation of alcohols to yield nitriles. This study provides a novel strategy for the green synthesis of nitriles, which sheds light on synthesizing more value-added products by selective oxidation processes.

## ASSOCIATED CONTENT

### Supporting Information

The Supporting Information is available free of charge at <https://pubs.acs.org/doi/10.1021/jacs.2c07061>.

Detailed experimental procedures of catalyst syntheses, characterizations, and the photocatalytic reaction; screening of photocatalysts and reaction condition optimization; detailed characterization and electrochemical and photoelectrochemical data of the  $\text{Fe}/\text{TiO}_2$  catalysts; reaction kinetics data; stability test results; photocatalytic activity under sunlight irradiation; and control experiments' data (PDF)

## AUTHOR INFORMATION

### Corresponding Authors

**Zehui Zhang** – School of Chemistry and Materials Science, South-Central Minzu University, Wuhan 430074, P. R. China; [orcid.org/0000-0003-1711-2191](https://orcid.org/0000-0003-1711-2191); Email: [zehuizh@mail.ustc.edu.cn](mailto:zehuizh@mail.ustc.edu.cn)

**Huai-Yong Zhu** – School of Chemistry and Physics, Queensland University of Technology, Brisbane, Queensland 4001, Australia; [orcid.org/0000-0002-1790-1599](https://orcid.org/0000-0002-1790-1599); Email: [hy.zhu@qut.edu.au](mailto:hy.zhu@qut.edu.au)

### Authors

**Chensheng Xian** – School of Chemistry and Materials Science, South-Central Minzu University, Wuhan 430074, P. R. China

**Jie He** – School of Chemistry and Materials Science, South-Central Minzu University, Wuhan 430074, P. R. China

**Yurong He** – School of Chemistry and Materials Science, South-Central Minzu University, Wuhan 430074, P. R. China

**Jiabao Nie** – School of Chemistry and Materials Science, South-Central Minzu University, Wuhan 430074, P. R. China

**Ziliang Yuan** – School of Chemistry and Materials Science, South-Central Minzu University, Wuhan 430074, P. R. China

**Jie Sun** – School of Chemistry and Materials Science, South-Central Minzu University, Wuhan 430074, P. R. China; [orcid.org/0000-0002-7798-3012](https://orcid.org/0000-0002-7798-3012)

**Wayde N. Martens** – School of Chemistry and Physics, Queensland University of Technology, Brisbane, Queensland 4001, Australia

**Jingzhong Qin** – School of Chemistry and Materials Science, South-Central Minzu University, Wuhan 430074, P. R. China

Complete contact information is available at: <https://pubs.acs.org/10.1021/jacs.2c07061>

### Author Contributions

<sup>§</sup>C.X. and J.H. contributed equally to this work.

### Notes

The authors declare no competing financial interest.

## ACKNOWLEDGMENTS

The authors thank the National Natural Science Foundation of China (21922513), Hubei Provincial Natural Science Foundation of China (2020CFA096), Fundamental Research Funds for Central Universities (CSZY22011, CZQ21008, and CZP20001), Scientific Research Fund of South-Central Minzu University (YZZ21005), and Knowledge Innovation Program of Wuhan-Shuguang Project (2022010801020411).

## REFERENCES

- (1) Liu, J. Z.; Zhang, C.; Zhang, Z. Y.; Wen, X. J.; Dou, X. D.; Wei, J. L.; Qiu, X.; Song, S.; Jiao, N. Nitromethane as a nitrogen donor in Schmidt-type formation of amides and nitriles. *Science* **2020**, *367*, 281–285.
- (2) Mu, Y.; Nguyen, T. T.; Koh, M. J.; Schrock, R. R.; Hoveyda, A. H. J. N. c. E- and Z-, di- and tri-substituted alkenyl nitriles through catalytic cross-metathesis. *Nat. Chem.* **2019**, *11*, 478–487.
- (3) Chen, Y.; Xu, L.; Jiang, Y.; Ma, D. Assembly of  $\alpha$ -(Hetero)aryl Nitriles via Copper-Catalyzed Coupling Reactions with (Hetero)aryl Chlorides and Bromides. *Angew. Chem., Int. Ed.* **2021**, *60*, 7082–7086.
- (4) Tukhtaev, H. B.; Ivanov, K. L.; Bezzubov, S. I.; Cheshkov, D. A.; Melnikov, M. Y.; Budynina, E. M. aza-Wittig Reaction with Nitriles: How Carbonyl Function Switches from Reacting to Activating. *Org. Lett.* **2019**, *21*, 1087–1092.
- (5) Ma, J.; Liu, H.; He, X.; Chen, Z.; Liu, Y.; Hou, C.; Sun, Z.; Chu, W. Ni-Catalyzed C-H Cyanation of (Hetero)arenes with 2-Cyanoisothiazolidine 1,1-Dioxide as a Cyanation Reagent. *Org. Lett.* **2021**, *23*, 2868–2872.
- (6) Yang, L.; Liu, Y.-T.; Park, Y.; Park, S.-W.; Chang, S. J. A. C. Ni-Mediated Generation of “CN” Unit from Formamide and Its Catalysis in the Cyanation Reactions. *ACS Catal.* **2019**, *9*, 3360–3365.
- (7) Feng, Y.; Long, S.; Tang, X.; Sun, Y.; Luque, R.; Zeng, X.; Lin, L. Earth-abundant 3d-transition-metal catalysts for lignocellulosic biomass conversion. *Chem. Soc. Rev.* **2021**, *50*, 6042–6093.

- (8) Fang, R.; Dhakshinamoorthy, A.; Li, Y.; Garcia, H. Metal organic frameworks for biomass conversion. *Chem. Soc. Rev.* **2020**, *49*, 3638–3677.
- (9) Qi, Z.; Hu, C.; Zhong, Y.; Cai, C.; Lu, G.-P. The ammoxidation of alcohols over heterogeneous catalysts for the green synthesis of nitriles. *Org. Chem. Front.* **2021**, *8*, 3137–3149.
- (10) Wang, Y.; Furukawa, S.; Fu, X.; Yan, N. J. A. C. Organonitrogen chemicals from oxygen-containing feedstock over heterogeneous catalysts. *ACS Catal.* **2019**, *10*, 311–335.
- (11) Sun, K.; Shan, H.; Neumann, H.; Lu, G. P.; Beller, M. Efficient iron single-atom catalysts for selective ammoxidation of alcohols to nitriles. *Nat. Commun.* **2022**, *13*, 1848.
- (12) Jagadeesh, R. V.; Junge, H.; Beller, M. Green synthesis of nitriles using non-noble metal oxides-based nanocatalysts. *Nat. Commun.* **2014**, *5*, 4123.
- (13) Han, P.; Tang, C.; Sarina, S.; Waclawik, E. R.; Du, A.; Bottle, S. E.; Fang, Y.; Huang, Y.; Li, K.; Zhu, H.-Y. Wavelength-Specific Product Desorption as a Key to Raising Nitrile Yield of Primary Alcohol Ammoxidation over Illuminated Pd Nanoparticles. *ACS Catal.* **2022**, *12*, 2280–2289.
- (14) Sun, K.-k.; Sun, J.-l.; Lu, G.-P.; Cai, C. Enhanced catalytic activity of cobalt nanoparticles encapsulated with an N-doped porous carbon shell derived from hollow ZIF-8 for efficient synthesis of nitriles from primary alcohols in water. *Green Chem.* **2019**, *21*, 4334–4340.
- (15) Qi, M. Y.; Conte, M.; Anpo, M.; Tang, Z. R.; Xu, Y. J. Cooperative Coupling of Oxidative Organic Synthesis and Hydrogen Production over Semiconductor-Based Photocatalysts. *Chem. Rev.* **2021**, *121*, 13051–13085.
- (16) Marzo, L.; Pagire, S. K.; Reiser, O.; König, B. Visible-Light Photocatalysis: Does It Make a Difference in Organic Synthesis? *Angew. Chem., Int. Ed.* **2018**, *57*, 10034–10072.
- (17) Verma, F.; Shukla, P.; Bhardiya, S. R.; Singh, M.; Rai, A.; Rai, V. K. Visible light-induced direct conversion of aldehydes into nitriles in aqueous medium using Co@g-C<sub>3</sub>N<sub>4</sub> as photocatalyst. *Catal. Commun.* **2019**, *119*, 76–81.
- (18) Nandi, J.; Leadbeater, N. E. Visible-light-driven catalytic oxidation of aldehydes and alcohols to nitriles by 4-acetamido-TEMPO using ammonium carbamate as a nitrogen source. *Org. Biomol. Chem.* **2019**, *17*, 9182–9186.
- (19) Shee, M.; Shah, S. S.; Singh, N. D. P. Photocatalytic Conversion of Benzyl Alcohols/Methyl Arenes to Aryl Nitriles via H-Abstraction by Azide Radical. *Chem.—Eur. J.* **2020**, *26*, 14070–14074.
- (20) Shayegan, Z.; Lee, C.-S.; Haghighat, F. TiO<sub>2</sub> photocatalyst for removal of volatile organic compounds in gas phase - A review. *Chem. Eng. J.* **2018**, *334*, 2408–2439.
- (21) Wu, X.; Li, J.; Xie, S.; Duan, P.; Zhang, H.; Feng, J.; Zhang, Q.; Cheng, J.; Wang, Y. Selectivity Control in Photocatalytic Valorization of Biomass-Derived Platform Compounds by Surface Engineering of Titanium Oxide. *Chem* **2020**, *6*, 3038–3053.
- (22) Shakeel Ahmad, M.; Pandey, A. K.; Abd Rahim, N. Advancements in the development of TiO<sub>2</sub> photoanodes and its fabrication methods for dye sensitized solar cell (DSSC) applications. A review. *Renewable Sustainable Energy Rev.* **2017**, *77*, 89–108.
- (23) Zhou, X.; Liu, N.; Schmuki, P. Photocatalysis with TiO<sub>2</sub> Nanotubes: “Colorful” Reactivity and Designing Site-Specific Photocatalytic Centers into TiO<sub>2</sub> Nanotubes. *ACS Catal.* **2017**, *7*, 3210–3235.
- (24) Bo, Y.; Wang, H.; Lin, Y.; Yang, T.; Ye, R.; Li, Y.; Hu, C.; Du, P.; Hu, Y.; Liu, Z.; Long, R.; Gao, C.; Ye, B.; Song, L.; Wu, X.; Xiong, Y. Altering Hydrogenation Pathways in Photocatalytic Nitrogen Fixation by Tuning Local Electronic Structure of Oxygen Vacancy with Dopant. *Angew. Chem., Int. Ed.* **2021**, *60*, 16085–16092.
- (25) Valero-Romero, M. J.; Santaclara, J. G.; Oar-Arteta, L.; van Koppen, L.; Osadchii, D. Y.; Gascon, J.; Kapteijn, F. Photocatalytic properties of TiO<sub>2</sub> and Fe-doped TiO<sub>2</sub> prepared by metal organic framework-mediated synthesis. *Chem. Eng. J.* **2019**, *360*, 75–88.
- (26) Cheng, G.; Liu, X.; Song, X.; Chen, X.; Dai, W.; Yuan, R.; Fu, X. Visible-light-driven deep oxidation of NO over Fe doped TiO<sub>2</sub> catalyst: Synergic effect of Fe and oxygen vacancies. *Appl. Catal., B* **2020**, *277*, 119196.
- (27) Xie, J.; Jin, R.; Li, A.; Bi, Y.; Ruan, Q.; Deng, Y.; Zhang, Y.; Yao, S.; Sankar, G.; Ma, D.; Tang, J. Highly selective oxidation of methane to methanol at ambient conditions by titanium dioxide-supported iron species. *Nat. Catal.* **2018**, *1*, 889–896.
- (28) Soltys-Mróz, M.; Syrek, K.; Pierzchała, J.; Wiercigroch, E.; Malek, K.; Sulka, G. D. Band gap engineering of nanotubular Fe<sub>2</sub>O<sub>3</sub>-TiO<sub>2</sub> photoanodes by wet impregnation. *Appl. Surf. Sci.* **2020**, *517*, 146195.
- (29) Choi, W.; Termin, A.; Hoffmann, M. R. The Role of Metal Ion Dopants in Quantum-Sized TiO<sub>2</sub>: Correlation between Photo-reactivity and Charge Carrier Recombination Dynamics. *J. Phys. Chem. A* **2002**, *98*, 13669–13679.
- (30) Zhang, Z.; Wu, Q.; Johnson, G.; Ye, Y.; Li, X.; Li, N.; Cui, M.; Lee, J. D.; Liu, C.; Zhao, S.; Li, S.; Orlov, A.; Murray, C. B.; Zhang, X.; Gunnoe, T. B.; Su, D.; Zhang, S. Generalized Synthetic Strategy for Transition-Metal-Doped Brookite-Phase TiO<sub>2</sub> Nanorods. *J. Am. Chem. Soc.* **2019**, *141*, 16548–16552.
- (31) Shen, G.; Zhang, R.; Pan, L.; Hou, F.; Zhao, Y.; Shen, Z.; Mi, W.; Shi, C.; Wang, Q.; Zhang, X.; Zou, J. J. Regulating the Spin State of Fe III by Atomically Anchoring on Ultrathin Titanium Dioxide for Efficient Oxygen Evolution Electrocatalysis. *Angew. Chem., Int. Ed. Engl.* **2020**, *59*, 2313–2317.
- (32) Jia, P.; Li, Q.; Poh, W. C.; Jiang, H.; Liu, H.; Deng, H.; Wu, J. Light-Promoted Bromine-Radical-Mediated Selective Alkylation and Amination of Unactivated C(sp<sup>3</sup>)-H Bonds. *Chem* **2020**, *6*, 1766–1776.
- (33) Talukdar, R. Tracking down the brominated single electron oxidants in recent organic red-ox transformations: photolysis and photocatalysis. *Org. Biomol. Chem.* **2020**, *18*, 8294–8345.
- (34) Hua, M.; Song, J.; Huang, X.; Liu, H.; Fan, H.; Wang, W.; He, Z.; Liu, Z.; Han, B. Highly Efficient Oxidative Cyanation of Aldehydes to Nitriles over Se,S,N- tri -Doped Hierarchically Porous Carbon Nanosheets. *Angew. Chem., Int. Ed.* **2021**, *60*, 21479–21485.
- (35) Sun, X.; Luo, X.; Zhang, X.; Xie, J.; Jin, S.; Wang, H.; Zheng, X.; Wu, X.; Xie, Y. Enhanced Superoxide Generation on Defective Surfaces for Selective Photooxidation. *J. Am. Chem. Soc.* **2019**, *141*, 3797–3801.
- (36) Wang, H.; Sun, X.; Li, D.; Zhang, X.; Chen, S.; Shao, W.; Tian, Y.; Xie, Y. Boosting Hot-Electron Generation: Exciton Dissociation at the Order-Disorder Interfaces in Polymeric Photocatalysts. *J. Am. Chem. Soc.* **2017**, *139*, 2468–2473.
- (37) Guo, Q.; Zhou, C.; Ma, Z.; Yang, X. Fundamentals of TiO<sub>2</sub> Photocatalysis: Concepts, Mechanisms, and Challenges. *Adv. Mater.* **2019**, *31*, 1901997.
- (38) Li, Z.; Luo, L.; Li, M.; Chen, W.; Liu, Y.; Yang, J.; Xu, S. M.; Zhou, H.; Ma, L.; Xu, M.; Kong, X.; Duan, H. Photoelectrocatalytic C-H halogenation over an oxygen vacancy-rich TiO<sub>2</sub> photoanode. *Nat. Commun.* **2021**, *12*, 6698.
- (39) Zhu, Z.; Huang, H.; Liu, L.; Chen, F.; Tian, N.; Zhang, Y.; Yu, H. Chemically Bonded alpha-Fe<sub>2</sub>O<sub>3</sub>/Bi<sub>4</sub>Mo<sub>8</sub>Cl Dot-on-Plate Z-Scheme Junction with Strong Internal Electric Field for Selective Photo-oxidation of Aromatic Alcohols. *Angew. Chem., Int. Ed.* **2022**, *61*, No. e202203519.
- (40) Parrino, F.; Camera Roda, G.; Loddò, V.; Palmisano, L. Elemental Bromine Production by TiO<sub>2</sub> Photocatalysis and/or Ozonation. *Angew. Chem., Int. Ed.* **2016**, *55*, 10391–10395.
- (41) Maurino, V.; Minella, M.; Sordello, F.; Minero, C. A proof of the direct hole transfer in photocatalysis: The case of melamine. *Appl. Catal., A* **2016**, *521*, 57–67.
- (42) Pan, C.; Fu, L.; Lide, F.; Ding, Y.; Wang, C.; Huang, J.; Wang, S. Insights into bromate reduction by Fe(II): Multiple radicals generation and carbamazepine oxidation. *Chem. Eng. J.* **2022**, *431*, 133957.
- (43) Treinin, A.; Hayon, E. Charge transfer spectra of halogen atoms in water. Correlation of the electronic transition energies of iodine, bromine, chlorine, hydroxyl, and hydrogen radicals with their electron affinities. *J. Am. Chem. Soc.* **1975**, *97*, 1716–1721.

(44) Guo, K.; Zheng, S.; Zhang, X.; Zhao, L.; Ji, S.; Chen, C.; Wu, Z.; Wang, D.; Fang, J. Roles of Bromine Radicals and Hydroxyl Radicals in the Degradation of Micropollutants by the UV/Bromine Process. *Environ. Sci. Technol.* **2020**, *54*, 6415–6426.

(45) Murugesan, K.; Donabauer, K.; König, B. J. A. C. I. E. Visible-Light-Promoted Metal-Free Synthesis of (Hetero)Aromatic Nitriles from C(sp<sup>3</sup>)-H Bonds\*\*. *Angew. Chem., Int. Ed.* **2021**, *60*, 2439–2445.

(46) Song, S.; Wang, Y.; Yan, N. A remarkable solvent effect on reductive amination of ketones. *Mol. Catal.* **2018**, *454*, 87–93.

(47) Wang, Y.; Furukawa, S.; Zhang, Z.; Torrente-Murciano, L.; Khan, S. A.; Yan, N. Oxidant free conversion of alcohols to nitriles over Ni-based catalysts. *Catal. Sci. Technol.* **2019**, *9*, 86–96.

(48) Padwa, A.; Rosenthal, R. J.; Dent, W.; Filho, P.; Turro, N. J.; Hrovat, D. A.; Gould, I. R. Steady-state and laser photolysis studies of substituted 2H-azirines. Spectroscopy, absolute rates, and Arrhenius behavior for the reaction of nitrile ylides with electron deficient olefins. *J. Org. Chem.* **1984**, *49*, 3174–3180.

(49) Zhang, M.; Wang, Q.; Chen, C.; Zang, L.; Ma, W.; Zhao, J. Oxygen Atom Transfer in the Photocatalytic Oxidation of Alcohols by TiO<sub>2</sub>: Oxygen Isotope Studies. *Angew. Chem., Int. Ed.* **2009**, *48*, 6081–6084.

(50) Li, H.; Qin, F.; Yang, Z.; Cui, X.; Wang, J.; Zhang, L. New Reaction Pathway Induced by Plasmon for Selective Benzyl Alcohol Oxidation on BiOCl Possessing Oxygen Vacancies. *J. Am. Chem. Soc.* **2017**, *139*, 3513–3521.

(51) Itoh, A.; Hashimoto, S.; Kuwabara, K.; Kodama, T.; Masaki, Y. Facile solar oxidation of alcohols with molecular oxygen. *Green Chem.* **2005**, *7*, 830–832.

(52) Liu, C.; Liu, H.; Zheng, X.; Chen, S.; Lai, Q.; Zheng, C.; Huang, M.; Cai, K.; Cai, Z.; Cai, S. Visible-Light-Enabled Allylic C-H Oxidation: Metal-free Photocatalytic Generation of Enones. *ACS Catal.* **2022**, *12*, 1375–1381.

(53) Zhang, H.; Wang, W.; Zhao, H.; Zhao, L.; Gan, L.-Y.; Guo, L.-H. Facet-Dependent Interfacial Charge Transfer in Fe(III)-Grafted TiO<sub>2</sub> Nanostructures Activated by Visible Light. *ACS Catal.* **2018**, *8*, 9399–9407.

(54) Parrino, F.; Livraghi, S.; Giamello, E.; Ceccato, R.; Palmisano, L. Role of Hydroxyl, Superoxide, and Nitrate Radicals on the Fate of Bromide Ions in Photocatalytic TiO<sub>2</sub> Suspensions. *ACS Catal.* **2020**, *10*, 7922–7931.

(55) Zhu, P.; Zhang, J.; Wang, J.; Kong, P.; Wang, Y.; Zheng, Z. Photocatalytic selective aerobic oxidation of amines to nitriles over Ru/γ-Al<sub>2</sub>O<sub>3</sub>: the role of the support surface and the strong imine intermediate adsorption. *Catal. Sci. Technol.* **2020**, *10*, 440–449.

(56) Yasukawa, T.; Yang, X.; Kobayashi, S. Earth-Abundant Bimetallic Nanoparticle Catalysts for Aerobic Ammoxidation of Alcohols to Nitriles. *J. Org. Chem.* **2020**, *85*, 7543–7548.

## Supporting Information

### High Nitrile Yield of Aerobic Ammoxidation of Alcohols Achieved by Generating $\cdot\text{O}_2^-$ and $\text{Br}\cdot$ Radicals over Iron-Modified $\text{TiO}_2$ Photocatalysts

Chensheng Xian <sup>a,‡</sup>, Jie He <sup>a,‡</sup>, Yurong He <sup>a</sup>, Jiabao Nie <sup>a</sup>, Ziliang Yuan <sup>a</sup>, Jie Sun <sup>a</sup>, Wayne N Martens <sup>b</sup>, Jingzhong Qin <sup>a</sup>, Huai-Yong Zhu <sup>b,\*</sup>, and Zehui Zhang<sup>a,\*</sup>

<sup>a</sup> *School of Chemistry and Materials Science, South-Central Minzu University, Wuhan 430074, P. R. China.*

<sup>b</sup> *School of Chemistry and Physics, Queensland University of Technology, Brisbane, QLD 4001, Australia.*

\* *Email: Huai-Yong Zhu (hy.zhu@qut.edu.au), Zehui Zhang ([zehuizh@mail.ustc.edu.cn](mailto:zehuizh@mail.ustc.edu.cn)).*

<sup>‡</sup> *These authors contributed equally to this work.*

## 1. Experimental Section

**Materials.** All the chemicals used for the preparation of the substrates and the starting materials were purchased from Aladdin Chemicals Co. Ltd. (Beijing, China), and used as received. All the solvents were supplied from Sinopharm Chemical Reagent Co., Ltd. (Shanghai, China) and used directly without further purification.

**Synthesis of iron-modified titanium dioxide (Fe/TiO<sub>2</sub>).** According to a previous study with minor modifications, Fe/TiO<sub>2</sub> samples were prepared using an impregnation-calcination method.<sup>1</sup> Generally, anhydrous FeCl<sub>3</sub> was dissolved in 10 mL of deionized water to obtain a solution, and 1 g of commercial TiO<sub>2</sub> (P25, anatase/rutile = 80:20, Degussa) was dispersed in 50 mL of deionized water under sonication for 30 min. Subsequently, the FeCl<sub>3</sub> solution was added dropwise to the TiO<sub>2</sub> suspension under continuous stirring. The mixture was kept at room temperature for 12 h with stirring. Then, water was removed by heating the mixture at 70 °C under stirring for 12 h, and the solid was dried thoroughly in an oven at 70 °C overnight. Finally, the product was obtained by grinding the dried solid with a mortar for 30 min before calcining it in a muffle furnace at 400 °C for 4 h, with a heating rate of 5 °C/min. The samples were noted as Fe-x/TiO<sub>2</sub> (x represents the calculated mass ratio of iron to TiO<sub>2</sub>). For example, Fe-2.0/TiO<sub>2</sub> represents that the Fe/TiO<sub>2</sub> mass ratio is 2.0%.

**Synthesis of cadmium sulfide (CdS).** CdS was prepared according to the method in the literature.<sup>2</sup> 4.62 g of CdCl<sub>2</sub>·2.5H<sub>2</sub>O and 4.62 g of thiourea were dissolved in 60 mL of ethylenediamine under stirring for 30 min. The solution was transferred to a 100 mL autoclave with a Teflon lining and maintained at 160 °C for 24 h. Subsequently, the reactor was naturally cooled to room temperature, the suspension was centrifuged, and the precipitant was washed with deionized water and ethanol three times. The product was obtained after drying in an oven at 70 °C for 8 h.

**Synthesis of ceric oxide (CeO<sub>2</sub>).** CeO<sub>2</sub> was prepared according to a previous study.<sup>3</sup> Typically, 3.47 g of Ce(NO<sub>3</sub>)<sub>3</sub>·6H<sub>2</sub>O and 38.4 g of NaOH were dissolved in 20 mL and 140 mL of deionized water, respectively. Then the Ce(NO<sub>3</sub>)<sub>3</sub> solution was added dropwise to the NaOH solution, and the mixture was stirred at room temperature for 30 min. Subsequently, the suspension was transferred to an autoclave with a Teflon lining

and kept at 100 °C for 24 h. After naturally cooling to room temperature, the resulting product was centrifuged, washed repeatedly with deionized water, and dried in an oven at 70 °C. The product was finally obtained by calcination at 600 °C for 2 h in a muffle furnace, with a heating rate of 5 °C/min.

**Synthesis of bismuth vanadate (BiVO<sub>4</sub>).** BiVO<sub>4</sub> was synthesized according to a reported method.<sup>4</sup> 2.91 g of Bi(NO<sub>3</sub>)<sub>3</sub>·5H<sub>2</sub>O was dissolved in 30 mL of 1 M HNO<sub>3</sub> solution under stirring for 30 min. Then, 0.70 g of NH<sub>4</sub>VO<sub>3</sub> was added to the above solution. After 2 h, the mixture was transferred into an autoclave with a Teflon lining and kept at 70 °C for 15 h. After natural cooling to room temperature, the suspension was filtered and washed with deionized water and ethanol, respectively. The product was obtained after drying in an oven at 70 °C for 8 h.

**Synthesis of Co/TiO<sub>2</sub>, Ni/TiO<sub>2</sub>, Cu/TiO<sub>2</sub>, Fe/CdS, Fe/CeO<sub>2</sub>, and Fe/BiVO<sub>4</sub>.** Co/TiO<sub>2</sub>, Ni/TiO<sub>2</sub>, and Cu/TiO<sub>2</sub> were prepared using the same method as Fe/TiO<sub>2</sub> preparation, except that the metal precursors were CoCl<sub>2</sub>·6H<sub>2</sub>O, NiCl<sub>2</sub>·4H<sub>2</sub>O, CuCl<sub>2</sub>·2H<sub>2</sub>O, respectively. Fe/CdS, Fe/CeO<sub>2</sub>, and Fe/BiVO<sub>4</sub> were also prepared using the same procedures, except that the semiconductor photocatalyst was the *as*-prepared CdS, CeO<sub>2</sub>, and BiVO<sub>4</sub>, respectively. For all photocatalysts, the content of the doped metal in the photocatalysts was 2.0%.

**Characterization.** Powder X-ray diffraction (XRD) measurements were conducted with the Bruker D8 Advance instrument. X-ray photoelectron spectroscopy measurement was performed on a Thermo Scientific XPS K-alpha machine using monochromatic Al-K $\alpha$  radiation, with the peak of C 1s (284.8 eV) as the reference. Survey scans were conducted in the range of 0–1150 eV (binding energy) at pass energy of 100.0 eV, and the analysis was conducted using Avantage and XPS Peak software. Thanks to eceshi ([www.eceshi.com](http://www.eceshi.com)) for the Ar-sputtering XPS measurements, the surface of each sample was initially cleaned with Ar<sup>+</sup> ions (high purity 99.999%) sputtering at a beam energy of 2 kV under a chamber with a base pressure of less than  $1.0 \times 10^{-9}$  mBar. The STEM measurements were performed on a 300 kV Titan G2 60–300 microscope (FEI) equipped with a probe Cs-corrector and a super-X EDX detector (FEI) (Provided by shiyanjia ([www.shiyanjia.com](http://www.shiyanjia.com))). Specific surface areas were

measured using the Brunauer–Emmett–Teller (BET) method with N<sub>2</sub> adsorption, and the data were collected by a Micromeritics TriStar 3000 gas adsorption analyzer. NH<sub>3</sub> temperature-programmed desorption (NH<sub>3</sub>-TPD) was conducted on a BELCAT II Microtrac BEL instrument equipped with a thermal conductivity detector (TCD). UV-VIS absorption spectra were obtained on a Shimadzu UV-Vis 2550 spectrophotometer fitted with an integrating sphere. The reflection measurements were converted to the absorption spectra using Kubelka–Mulk transformation. Photoluminescence (PL) emission spectra of the samples were measured on a fluorescence spectrophotometer (Hitachi, Model F-7000) with an excitation wavelength of 250 nm at room temperature. Time-resolved PL fluorescence spectra were obtained using an FLS-1000 spectrometer (Edinburgh instruments) with an excitation wavelength of 375 nm and a probe wavelength of 410 nm. The electron paramagnetic resonance (EPR) signal was recorded on the Bruker EMX EPR spectrometer (Bruker, USA). Absorption spectra of Br<sub>2</sub><sup>•-</sup> by using a laser flash photolysis (LFP) spectrometer (LP980, Edinburgh Instruments Ltd., U.K.) equipped with a Continuum Surelite I-10 Q-switched Nd:YAG laser and the third harmonic (355 nm) of a Quanta Ray GCR Nd:YAG laser. Photoelectrochemical activity measurements, including photocurrent density and electrochemical impedance spectroscopy (EIS), were recorded employing an electrochemical analyzer (CHI660E, Shanghai Chenhua electrochemical workstation) over a standard three-electrode system using the to-be-measured sample coated on FTO glass as the working electrode, a Pt wire as the counter electrode, and Ag/AgCl as the reference electrode. Mott-Schottky experiments were performed in a sodium sulfate electrolyte solution (0.2 M) (pH = 6.8), and the perturbation signals were 10 mV at a frequency of 1 kHz. The content of Fe in the catalyst was determined by inductively coupled plasma atomic emission spectroscopy (ICP-AES VISTA-MPX).

**Photocatalytic reaction.** The photocatalytic reactions were performed using a 50 mL stainless steel photoreactor with a quartz window (Xi'an Taikang, China). In a typical run, 20 mg of photocatalyst, 50 mg of 4Å molecular sieve, 0.2 mmol of alcohol, 10 mL of anhydrous acetonitrile, and NH<sub>4</sub>Br were added to the photoreactor. The air in the photoreactor was first removed by freezing vacuum pumping. Then oxygen was filled

into the photoreactor and removed by freezing vacuum pumping. This procedure was repeated 5 times. Then, ammonia gas was supplied into the photoreactor for 600 seconds, and an oxygen balloon was connected to the reactor. After stirring for 30 min in the dark, a LED was turned on (0.5 cm away from the quartz window,  $\lambda = 365$  nm), and the photocatalytic reaction was started for a certain time. After the reaction, the products were quantitatively analyzed by gas chromatography using ethylbenzene as the internal standard.



## 2. Supporting Figures

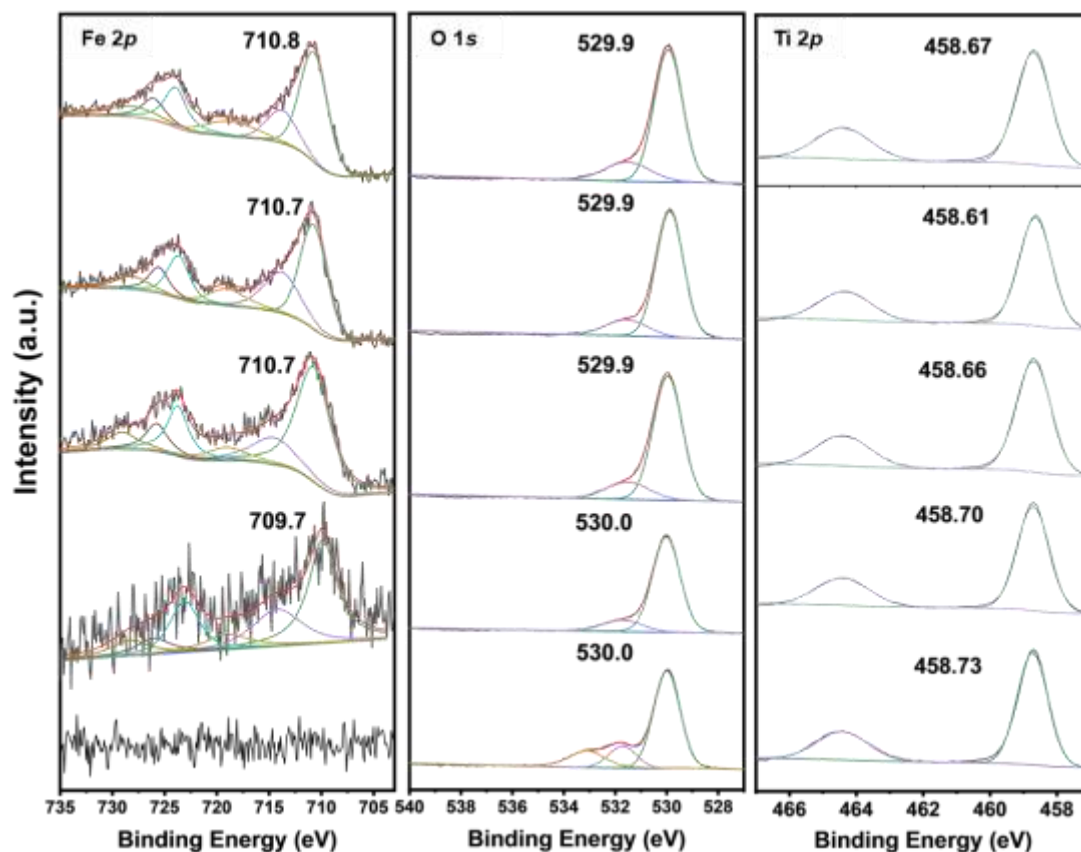


**Figure S1.** Fe 2p, O 1s, and Ti 2p XPS spectra of TiO<sub>2</sub>, Fe-0.3/TiO<sub>2</sub>, Fe-1.1/TiO<sub>2</sub>, Fe-2.0/TiO<sub>2</sub>, and Fe-6.0/TiO<sub>2</sub>.

Two peaks were deconvoluted from the O 1s spectrum (**Figure S1**). The most prominent peak with binding energy at 530.0 eV was attributed to the Ti–O bonds. The other O 1s peak with the binding energy at 531.5 eV was ascribed to the surface absorbed hydroxyl groups (–OH).<sup>5</sup>

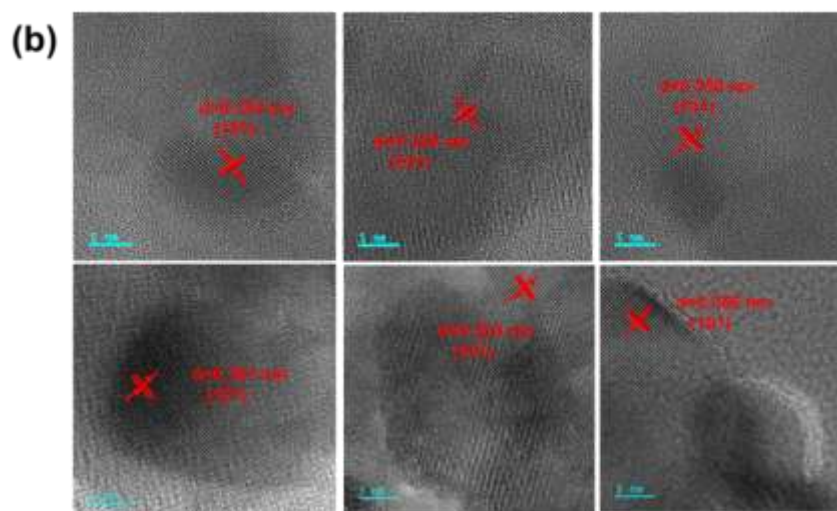
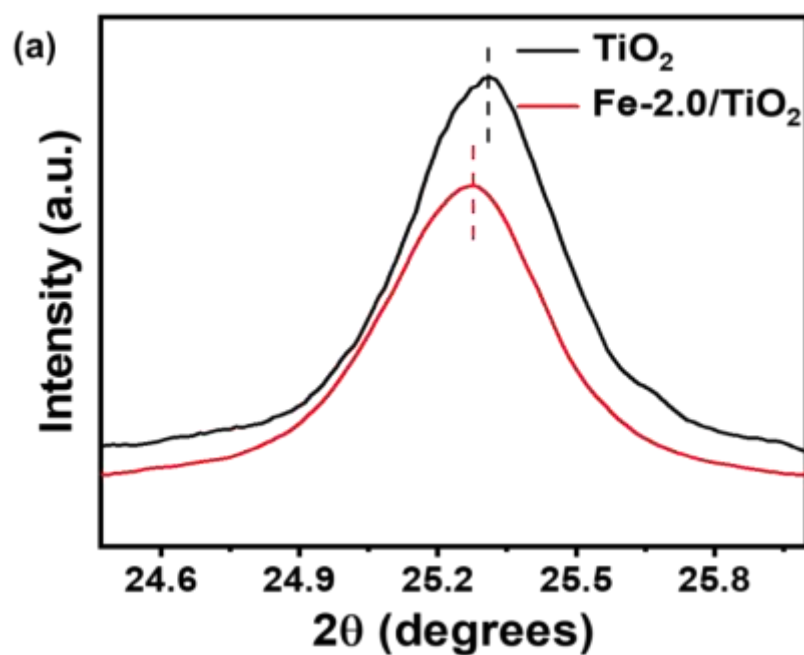


**Figure S2.** (a) Magnified X-Ray diffraction spectra of  $\text{TiO}_2$  and  $\text{Fe-2.0/TiO}_2$  in the range of  $10^\circ$  to  $30^\circ$  with a slow scan rate of  $2^\circ/\text{min}$  and (b) high-resolution TEM images of the  $\text{Fe-2.0/TiO}_2$  sample at different depths of view.

The characteristic X-ray diffraction peak corresponding to the (101) crystal plane is slightly shifted to a low angle compared to pristine  $\text{TiO}_2$  because  $\text{Ti}^{4+}$  was replaced by the  $\text{Fe}^{3+}$  (**Figure S2a**).<sup>6,7</sup>

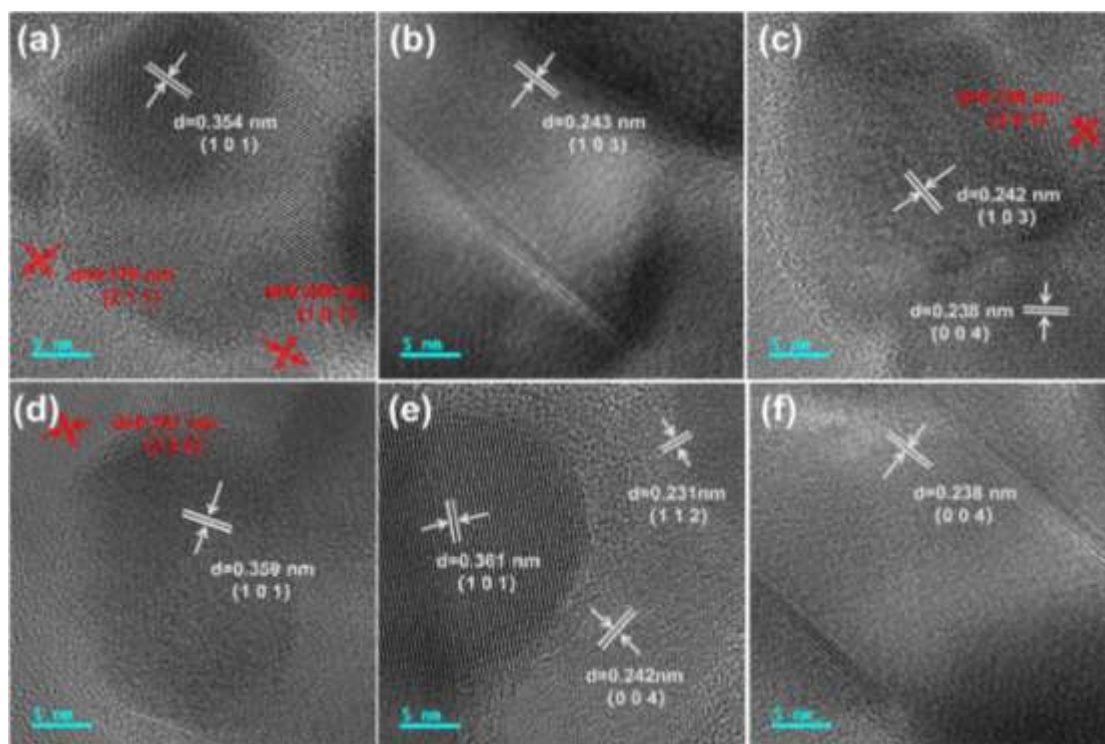


**Figure S3.** (a-c) HR-TEM images of Fe-0.3/TiO<sub>2</sub> and (d-f) Fe-0.3/TiO<sub>2</sub>-H<sub>2</sub>SO<sub>4</sub>.

The catalysts were obtained by treating Fe-0.3/TiO<sub>2</sub> with H<sub>2</sub>SO<sub>4</sub> to remove the tiny  $\alpha$ -Fe<sub>2</sub>O<sub>3</sub> nanoparticles on the surface of the TiO<sub>2</sub>. As shown in **Figure S3**,  $\alpha$ -Fe<sub>2</sub>O<sub>3</sub> nanoparticles were not visible in Fe-0.3/TiO<sub>2</sub> and Fe-0.3/TiO<sub>2</sub>-H<sub>2</sub>SO<sub>4</sub>.

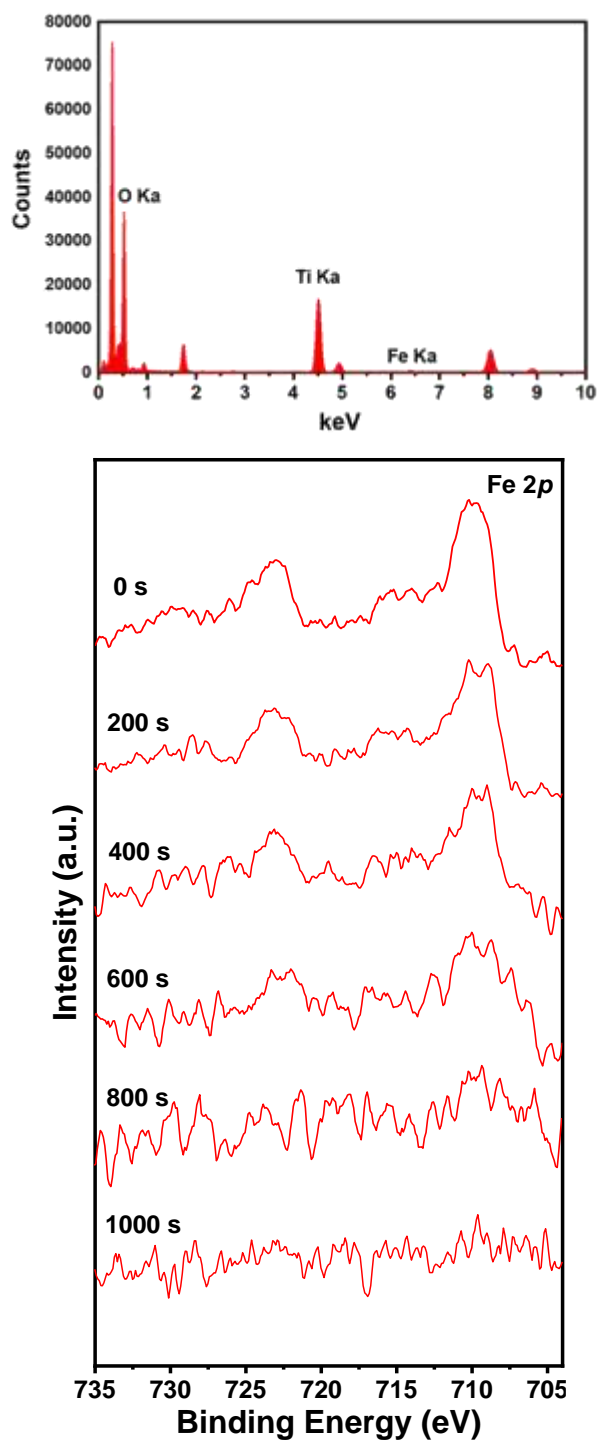


**Figure S4.** Energy dispersive x-ray spectroscopy of selected area of Fe-2.0/TiO<sub>2</sub> and XPS spectra of Fe 2*p* for Fe-2.0/TiO<sub>2</sub> during depth profile analysis. Sputtering time was 200, 400, 600, 800, and 1000 s.

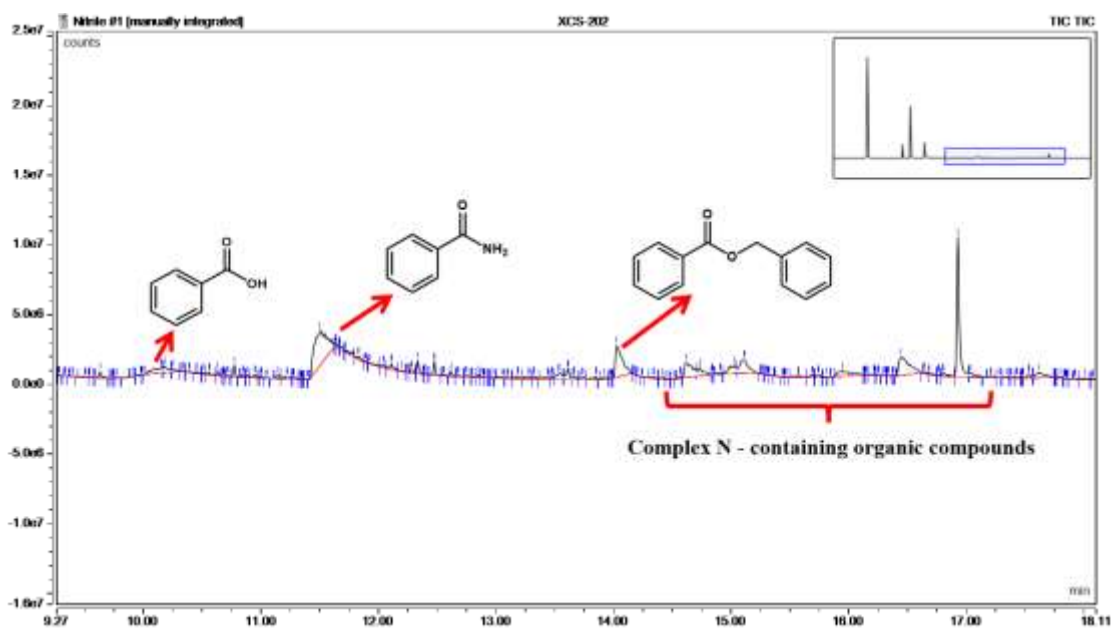
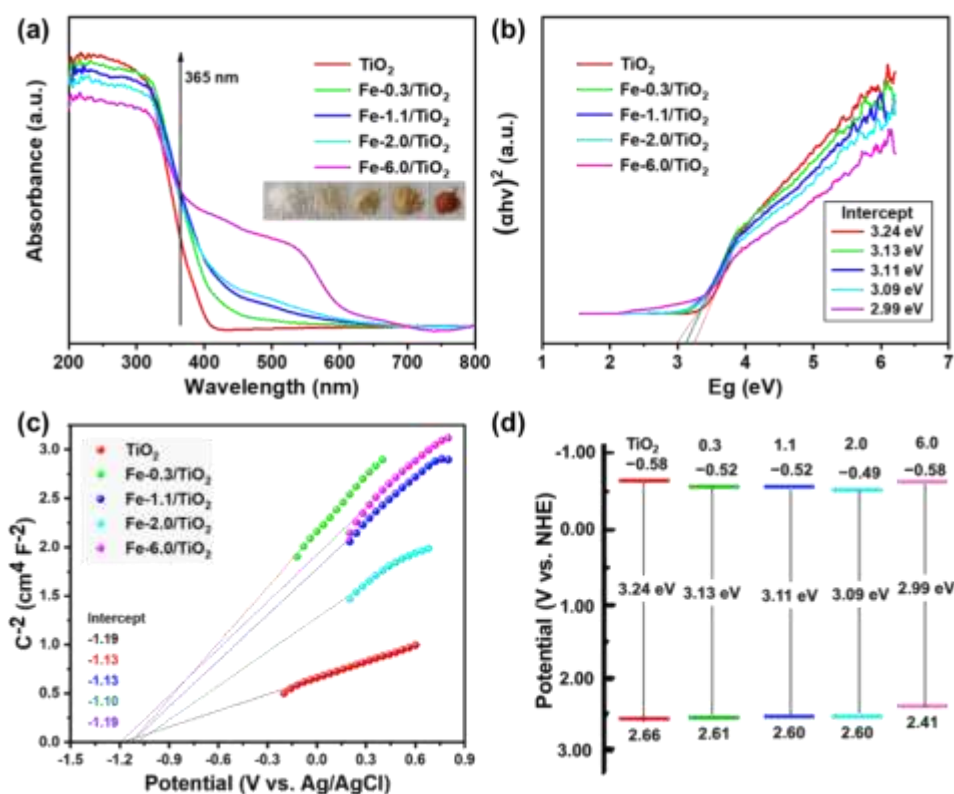


Figure S5. GC-MS analysis of by-products in the ammoxidation of alcohol to nitrile.



**Figure S6.** (a) Ultraviolet-visible diffuse reflectance spectra, (b) Tauc plots of  $\text{TiO}_2$ ,  $\text{Fe-0.3/TiO}_2$ ,  $\text{Fe-1.1/TiO}_2$ ,  $\text{Fe-2.0/TiO}_2$ , and  $\text{Fe-6.0/TiO}_2$ , (c) Mott–Schottky plots of interfacial capacitance derived from EIS data for  $\text{TiO}_2$ ,  $\text{Fe-0.3/TiO}_2$ ,  $\text{Fe-1.1/TiO}_2$ ,  $\text{Fe-2.0/TiO}_2$ , and  $\text{Fe-6.0/TiO}_2$  and (d) The conduction band and valence band positions of  $\text{TiO}_2$ ,  $\text{Fe-0.3/TiO}_2$ ,  $\text{Fe-1.1/TiO}_2$ ,  $\text{Fe-2.0/TiO}_2$ , and  $\text{Fe-6.0/TiO}_2$  calculated from the UV-vis absorption spectra and Mott-Schottky analyses.

#### Figure S6a,

Increasing the Fe loading to 6.0%,  $\alpha\text{-Fe}_2\text{O}_3$  formation caused a color change in the samples, from light yellow to dark yellow and finally to brown, which is the characteristic color of  $\alpha\text{-Fe}_2\text{O}_3$ . This suggests that in the  $\text{Fe-2.0/TiO}_2$  sample, the Fe(III) species reaches saturation in the  $\text{TiO}_2$  lattice, and any excess iron forms  $\alpha\text{-Fe}_2\text{O}_3$ .

The redox power of the semiconductor photocatalyst is directly associated with the band structure.<sup>8</sup> Thus, the bandgap of a series of  $\text{Fe-x/TiO}_2$  was studied. The diffuse reflection UV-VIS spectra of the  $\text{Fe-x/TiO}_2$  samples showed a redshift in the visible region compared to pristine  $\text{TiO}_2$ .

#### Figure S6b,

We calculated the bandgap energies of the samples from the Tauc plots using the Tauc

equation:  $(\alpha hv)^n = A(hv - E_g)$  where  $\alpha$ ,  $h$ ,  $\nu$ ,  $E_g$ , and  $A$  are the absorption coefficient, Planck constant, light frequency, bandgap, and a constant, respectively.<sup>9</sup> The Tauc plots demonstrated that the bandgap energies of the Fe- $x$ /TiO<sub>2</sub> samples became lower with increased iron content. The bandgap energies were calculated to be 3.24, 3.13, 3.11, 3.09, and 2.99 eV for TiO<sub>2</sub>, Fe-0.3/TiO<sub>2</sub>, Fe-1.1/TiO<sub>2</sub>, Fe-2.0/TiO<sub>2</sub> and Fe-6.0/TiO<sub>2</sub>, respectively. An absorption peak with the edge at ~600 nm was observed in the Fe-6.0/TiO<sub>2</sub> sample, ascribed to the absorption edge of  $\alpha$ -Fe<sub>2</sub>O<sub>3</sub>.

#### **Figure S6c,**

The electrochemical experiments were then carried out to investigate the band structure. The typical Mott-Schottky plots of the TiO<sub>2</sub> and Fe- $x$ /TiO<sub>2</sub> electrodes measured in the dark showed a positive slope of the  $C^{-2}$ - $E$  plot, characteristic of an n-type semiconductor. A flat-band potential ( $V_{fb}$ ) could be determined by extrapolating the linear part of the Mott-Schottky plot to the x-axis and was used to estimate the conduction band energy.

#### **Figure S6d,**

The valence band energies of TiO<sub>2</sub> and Fe(III) modified TiO<sub>2</sub> are more positive than those of other semiconductors. The light-generated holes can yield reactive species with sufficient oxidation power to oxidize the alcohol.<sup>8</sup>

Combining the bandgap energies calculated from the optical absorption (**Figure S6b**), we determined the valence band energies of TiO<sub>2</sub> and Fe- $x$ /TiO<sub>2</sub> samples (**Table S9 and Figure S6d**). The valence band energy of Fe- $x$ /TiO<sub>2</sub> samples, except the Fe-6.0/TiO<sub>2</sub> sample, became slightly less positive compared to TiO<sub>2</sub>, suggesting that the modification with Fe(III) species slightly weakened the photocatalytic oxidation power. This is consistent with the observation that the alcohol conversion over the Fe- $x$ /TiO<sub>2</sub> samples (except Fe-6.0/TiO<sub>2</sub>) is like that over TiO<sub>2</sub> (**Table 1**). Sufficient aerobic oxidation power is critical for this photocatalytic synthesis. The valence band decrease in the Fe-6.0/TiO<sub>2</sub> sample is ascribed to the valence band co-dominated by TiO<sub>2</sub> and  $\alpha$ -Fe<sub>2</sub>O<sub>3</sub>.

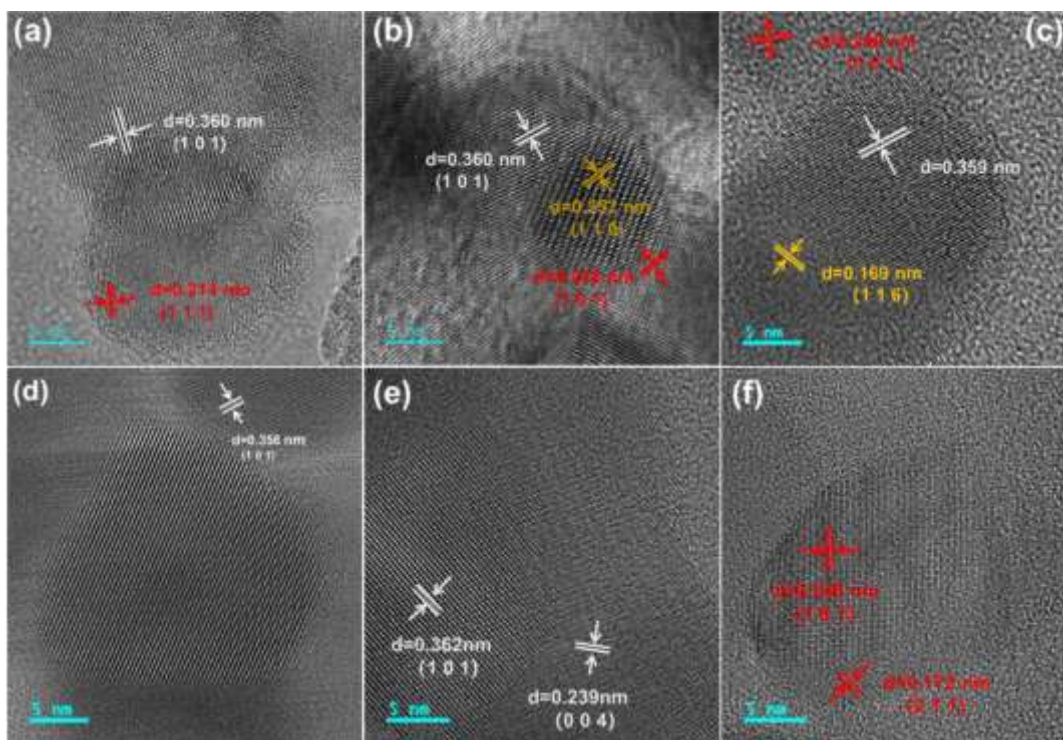


**Figure S7.** (a-c) HR-TEM images of Fe-2.0/TiO<sub>2</sub> and (d-f) Fe-2.0/TiO<sub>2</sub>-H<sub>2</sub>SO<sub>4</sub>.

The Fe-2.0/TiO<sub>2</sub>-H<sub>2</sub>SO<sub>4</sub> sample was obtained by treating Fe-2.0/TiO<sub>2</sub> with H<sub>2</sub>SO<sub>4</sub> to remove the tiny  $\alpha$ -Fe<sub>2</sub>O<sub>3</sub> nanoparticles on the surface of the TiO<sub>2</sub> (**Figure S7**).





**Figure S8.** The dissolution of ammonium bromide in acetonitrile.

We conducted the following experiment to evaluate the solubility of  $\text{NH}_4\text{Br}$  in  $\text{CH}_3\text{CN}$ . Typically, 5 mg of  $\text{NH}_4\text{Br}$  was accurately weighed and added into a beaker containing 30 mL of anhydrous  $\text{CH}_3\text{CN}$ . The mixture was ultrasonicated for 10 min, and the dissolution of ammonium bromide particles was observed and recorded.  $\text{NH}_4\text{Br}$  was not dissolved. Thus, 10 mL more of  $\text{CH}_3\text{CN}$  was added. This operation was repeated until no  $\text{NH}_4\text{Br}$  particles were seen. The solubility of  $\text{NH}_4\text{Br}$  in  $\text{CH}_3\text{CN}$  could be approximately calculated by the formula  $a=b/c$  where a, b and c represent the solubility of ammonium bromide, the mass of ammonium bromide, and the volume of acetonitrile, respectively.

As shown in the photographs below, when the accumulated volume of  $\text{CH}_3\text{CN}$  was 80 mL, very few ammonium bromide particles could be seen; at 90 mL, no noticeable ammonium bromide particles could be seen. Therefore, the approximate solubility of  $\text{NH}_4\text{Br}$  in acetonitrile is between 0.556 mg/10 mL and 0.625 mg/10 mL at room temperature.

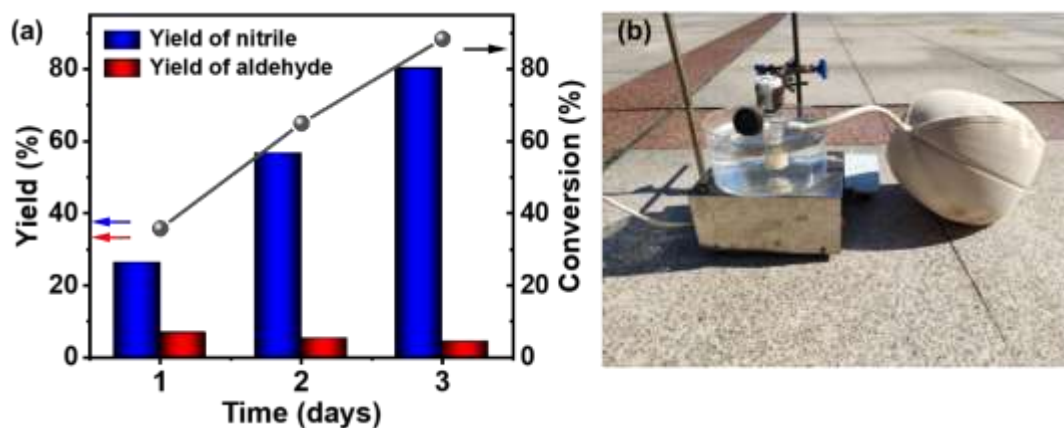


**Figure S9.** The experiment under natural sunlight.

To determine if the reaction could use sunlight, we conducted an experiment under three-day-time solar irradiation. (Reaction conditions: benzyl alcohol (0.2 mmol), photocatalyst (20 mg),  $\text{CH}_3\text{CN}$  (10 mL),  $4\text{\AA}$  MS (50 mg), an  $\text{NH}_3 + \text{O}_2$  balloon; Location:  $114^\circ40'03''\text{E}$ ,  $30.49026\text{N}$ , Wuhan, Hubei, China; Time: 9:00 am to 6:00 pm, August 1st to 3rd, 2022, with a total sunlight irradiation time of 27 hours). As shown in **Figure S9**, a good nitrile yield of 80.3% was achieved, demonstrating that the photocatalytic ammoxidation system in this work has solar applicability.

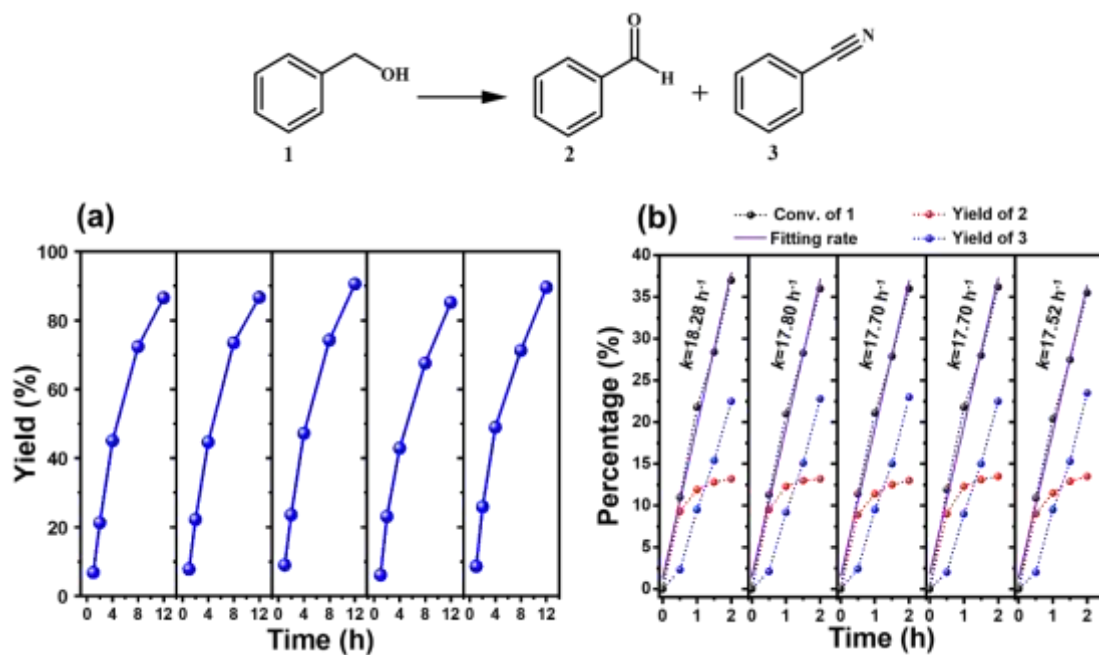


**Figure S10.** (a) The yield of nitriles in the recycling performance of Fe-2.0/TiO<sub>2</sub> photocatalyst and (b) the initial oxidation rates and the temporal profile of product formation during the recycling of the Fe-2.0/TiO<sub>2</sub> catalyst.

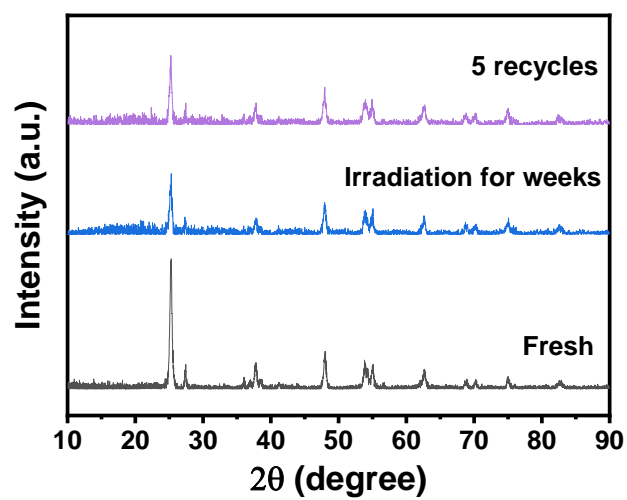


**Figure S11.** XRD patterns of catalyst Fe-2.0/TiO<sub>2</sub> after five recycles, irradiation for 2 weeks and as prepared fresh catalyst.

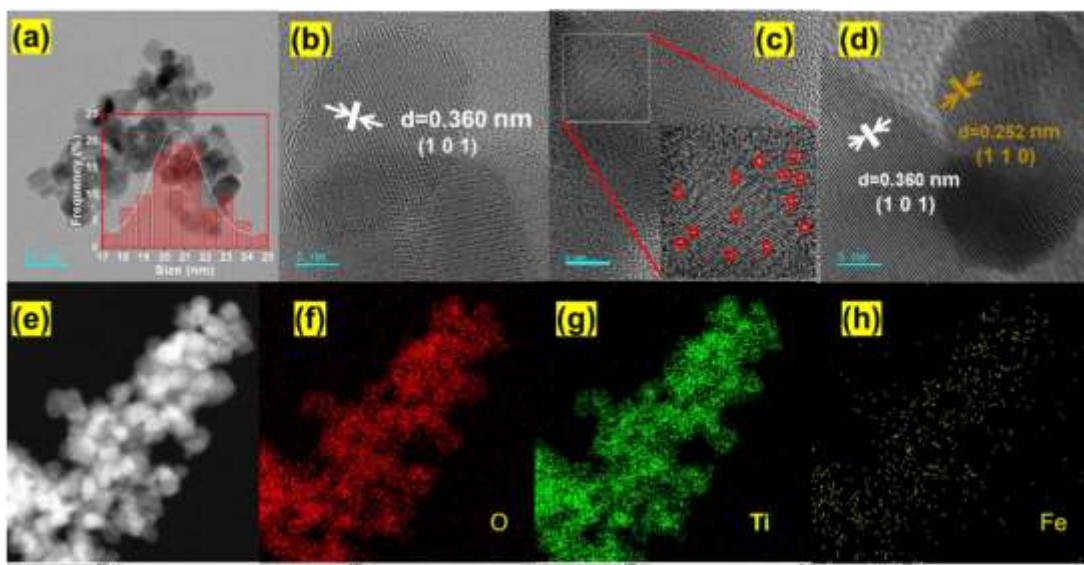


**Figure S12.** (a-b) The TEM images (the insert is the particle size distribution), (c-d) HRTEM images, and (e-h) elemental maps of the Fe-2.0/TiO<sub>2</sub> after five recycles.

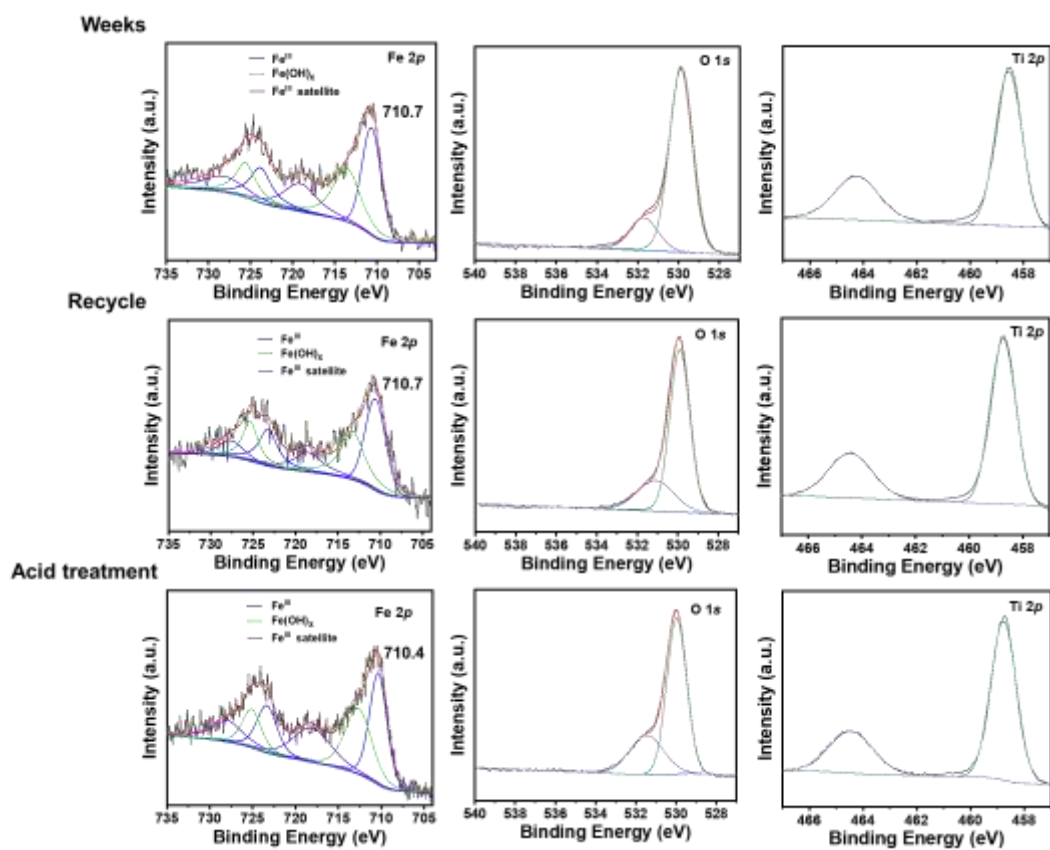


**Figure S13.** XPS spectra and corresponding fitted curves of the Fe-2.0/TiO<sub>2</sub> catalyst collected after being irradiated for 2 weeks, the Fe-2.0/TiO<sub>2</sub> catalyst collected after being recycled 5 times, and the Fe-2.0/TiO<sub>2</sub>-H<sub>2</sub>SO<sub>4</sub> sample.

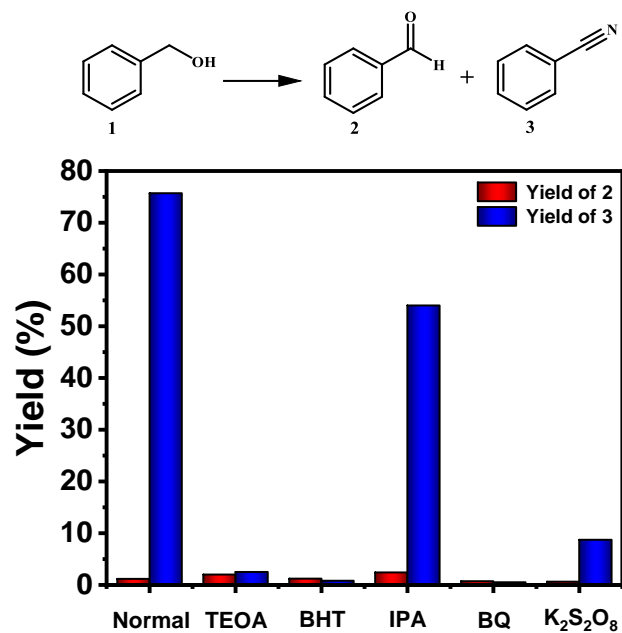


**Figure S14.** Photocatalytic conversion of benzyl alcohol to benzonitrile with different scavengers. Reaction conditions: benzyl alcohol (0.2 mmol), Fe-2.0/TiO<sub>2</sub> (20 mg), CH<sub>3</sub>CN (10 mL), 4Å MS (50 mg), NH<sub>4</sub>Br (1.0 eq.), NH<sub>3</sub> (0.1 MPa), O<sub>2</sub> balloon, LEDs (365 nm), scavenger (1 mmol), 12 h.

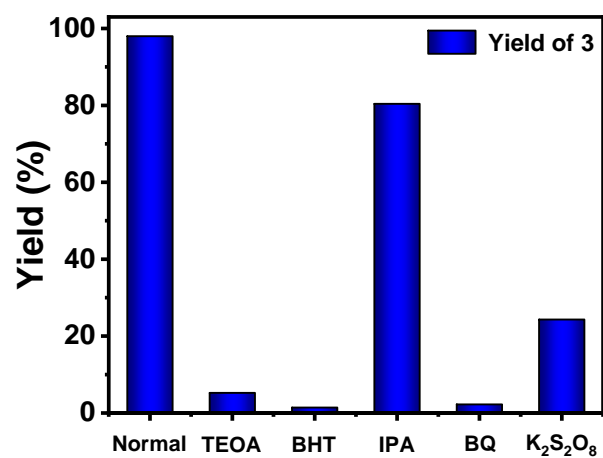
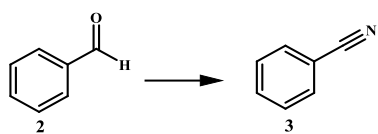


**Figure S15.** Photocatalytic conversion of benzaldehyde to benzonitrile with different scavengers. Reaction conditions: benzaldehyde (0.2 mmol), Fe-2.0/TiO<sub>2</sub> (20 mg), CH<sub>3</sub>CN (10 mL), 4Å MS (50 mg), NH<sub>4</sub>Br (1.0 eq.), NH<sub>3</sub> (0.1 MPa), O<sub>2</sub> balloon, LEDs (365 nm), scavenger (1 mmol), 12 h.



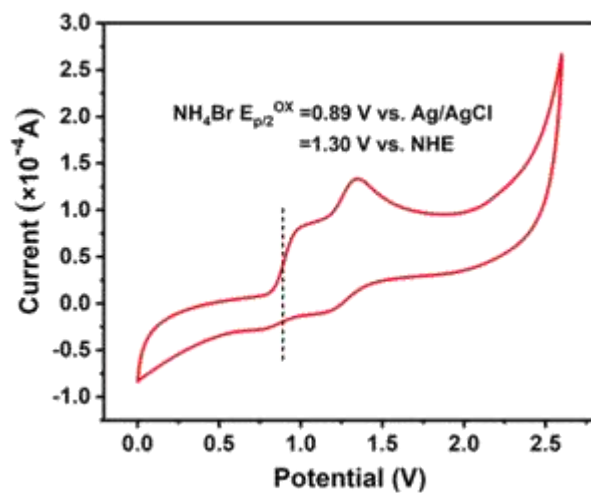


**Figure S16.** Cyclic voltammetry of  $\text{NH}_4\text{Br}$  ( $\text{NH}_4\text{Br}$  and tetrabutylammonium hexafluorophosphate in  $\text{CH}_3\text{CN}$  was used for tests).

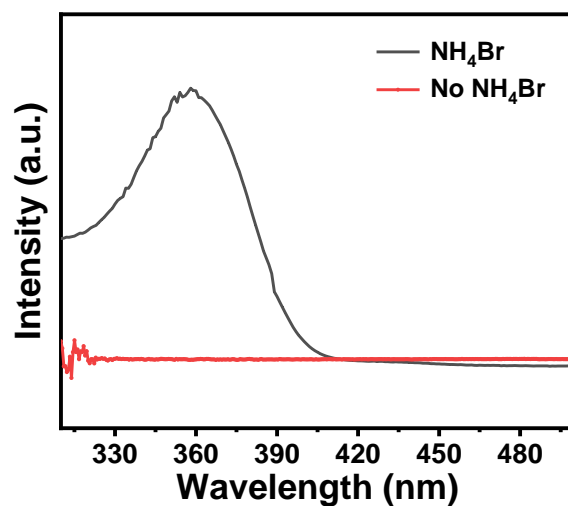


**Figure S17.** The absorption spectra under laser flash photolysis. Conditions: take 1 mmol NH<sub>4</sub>Br, 2 mg catalyst and 10 mL of deionized water, and ultrasonically treatment for 1 h.

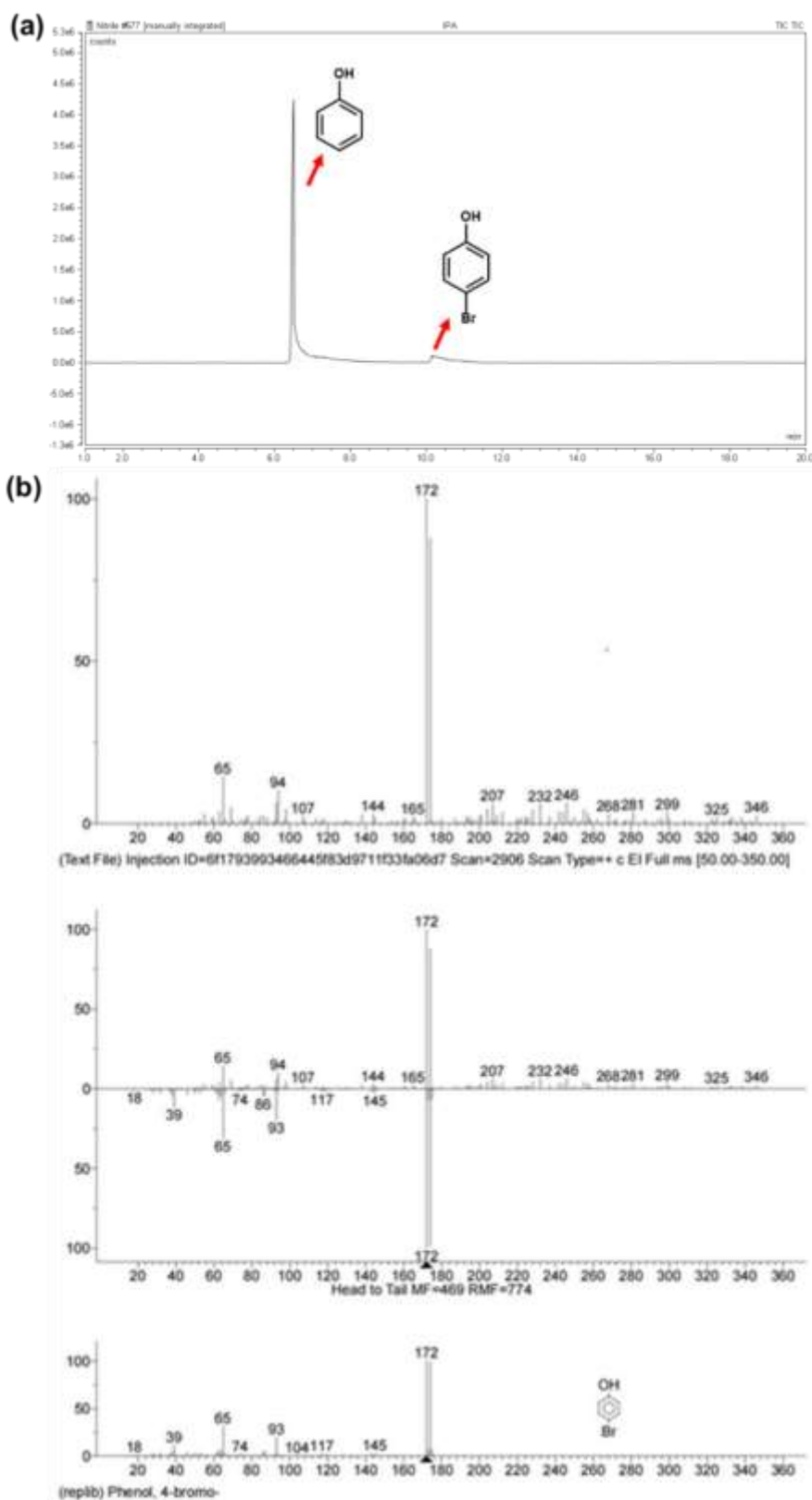


**Figure S18.** (a) The GC chromatogram of Bromine substitution reactions under standard conditions, except without ammonia and using phenol as substrate, and (b) The MS analysis of Bromine substitution product.

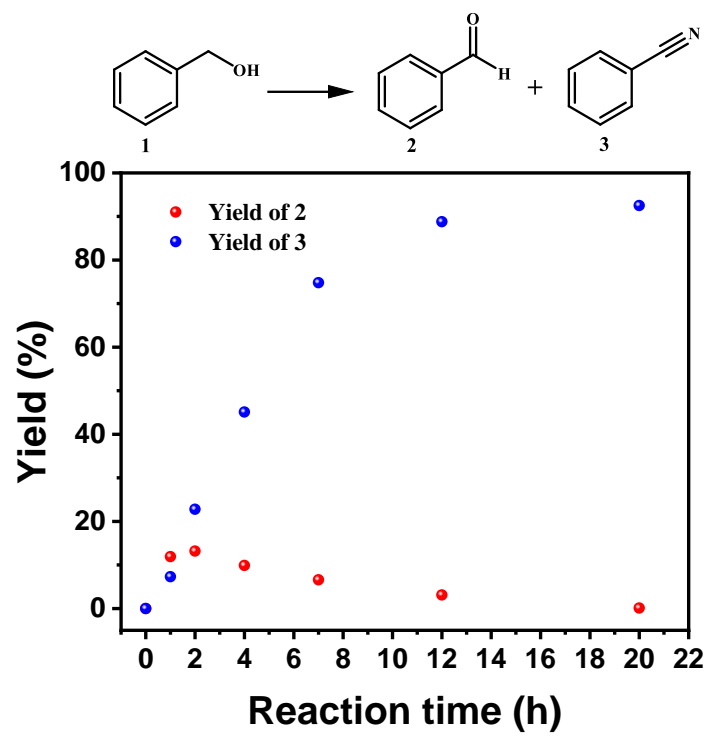


**Figure S19.** The yield of benzaldehyde and benzonitrile over time.

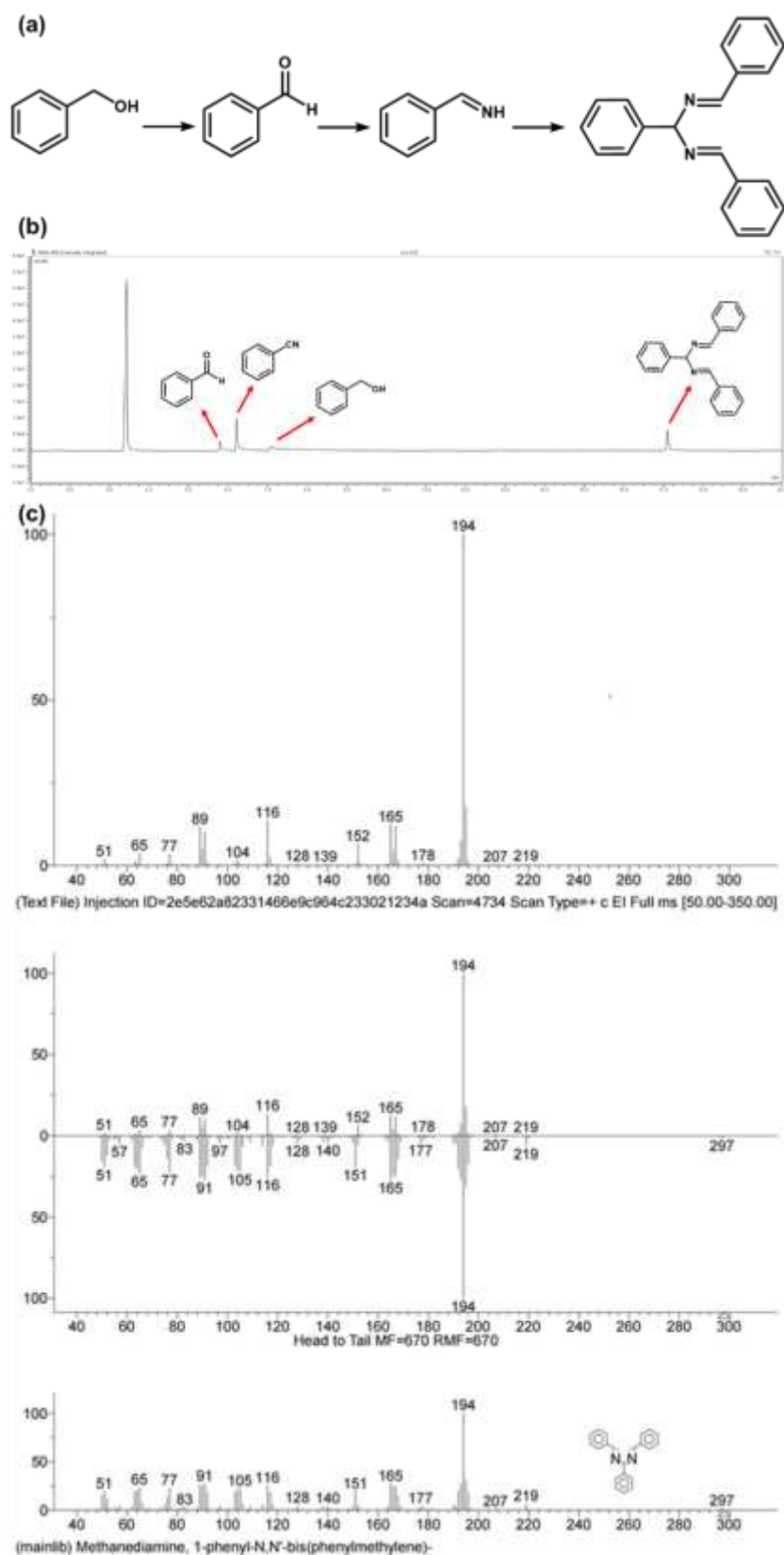


**Figure S20.** (a) The reaction path with pressured  $\text{NH}_3$  (1.0 Mpa), (b) the GC chromatogram of a condensation product, and (c) the MS analysis of condensation product.

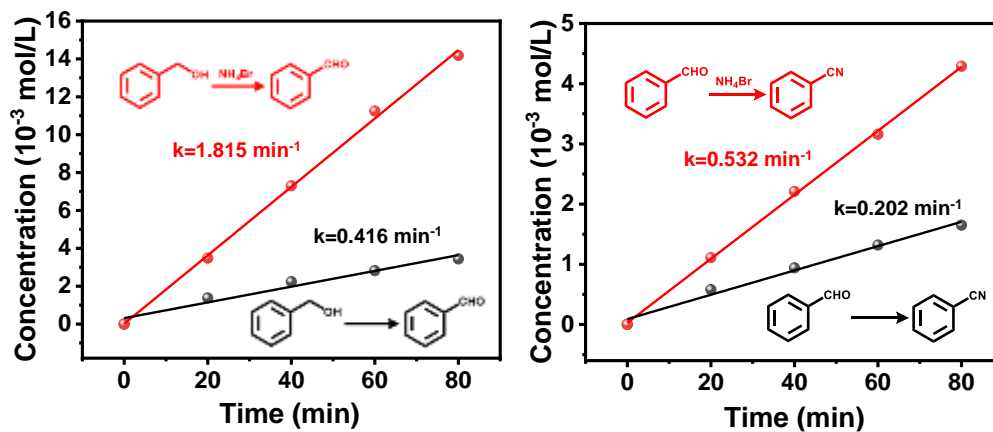


**Figure S21.** The rate of aerobic oxidation of alcohols to aldehydes and aldehydes ammoxidation to nitriles in the initial reaction stage.

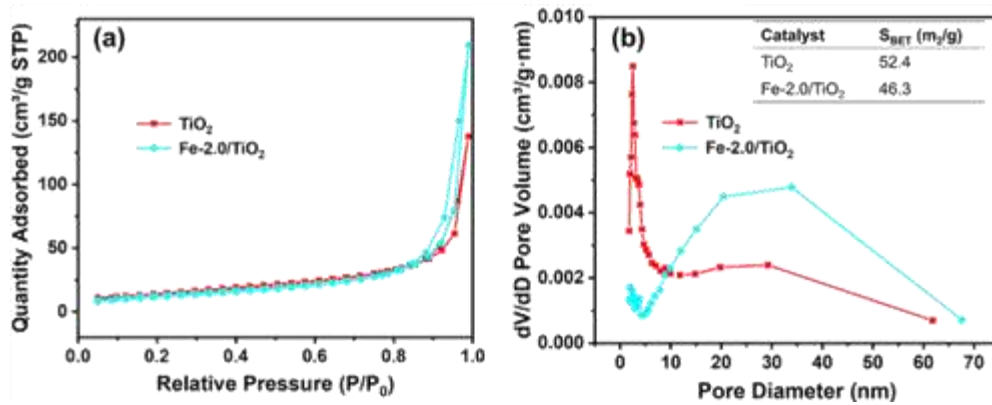


**Figure S22.** (a) Nitrogen adsorption/desorption isotherms and (b) pore diameter distribution (inserted BET surface area) of  $\text{TiO}_2$  and  $\text{Fe-2.0/TiO}_2$ .

### 3. Supporting Tables


**Table S1.** The effect of photocatalyst, light, and O<sub>2</sub> on product formation.

Entry	Deviation	Conv. (%)	Sel. of nitrile (%)
1	Without photocatalyst	0	0
2	Without light illumination	0	0
3	N <sub>2</sub> instead of O <sub>2</sub>	trace	trace

Reaction conditions: benzyl alcohol (0.2 mmol), photocatalyst (20 mg), CH<sub>3</sub>CN (10 mL), 4Å MS (50 mg), NH<sub>3</sub> (0.1 MPa), O<sub>2</sub> balloon, 365 nm LED, 12 h, room temperature.



**Table S2.** Control experiments on the ammoxidation reactions with different photocatalysts under variable conditions.



The image shows two chemical reaction schemes. The first scheme shows the conversion of benzyl alcohol (labeled 1) to benzaldehyde (labeled 2) and benzonitrile (labeled 3). The second scheme shows the conversion of benzaldehyde (labeled 2) to benzonitrile (labeled 3).

Entry	Substrate	Photocatalyst	Conv.(%)	Yield of nitrile (%)
1 <sup>a</sup>	Benzyl alcohol	TiO <sub>2</sub>	52.2	0
2 <sup>a</sup>	Benzyl alcohol	Fe-2.0/ TiO <sub>2</sub>	50.4	0
3 <sup>b</sup>	Benzyl alcohol	TiO <sub>2</sub>	49.2	4.3
4 <sup>b</sup>	Benzyl alcohol	Fe-2.0/ TiO <sub>2</sub>	49.6	36.6
5 <sup>b</sup>	Benzaldehyde	TiO <sub>2</sub>	>99	Trace
6 <sup>b</sup>	Benzaldehyde	Fe-2.0/ TiO <sub>2</sub>	75.5	43.0

Reaction conditions: substrate (0.2 mmol), photocatalyst (20 mg), CH<sub>3</sub>CN (10 mL), 4Å MS (50 mg), O<sub>2</sub> balloon, 365 nm LED, 12 h, room temperature. a) without NH<sub>3</sub>, b) NH<sub>3</sub> (0.1 MPa).

**Table S3.** Control experiments over Fe-2.0/TiO<sub>2</sub>, Fe-2.0/CeO<sub>2</sub>, Fe-2.0/CdS, and Fe-2.0/BiVO<sub>4</sub>.

Entry	Photocatalyst	Conv. (%)	Yield of aldehyde (%)	Yield of nitrile (%)
1 <sup>a</sup>	Fe-2.0/TiO <sub>2</sub>	49.6	8.5	36.6
2 <sup>b</sup>	Fe-2.0/TiO <sub>2</sub>	47.7	36.5	--
3 <sup>a</sup>	Fe-2.0/CeO <sub>2</sub>	3.1	1.2	1.9
4 <sup>b</sup>	Fe-2.0/CeO <sub>2</sub>	35.5	35.5	--
5 <sup>a</sup>	Fe-2.0/CdS	N.R.	N.D.	N.D.
6 <sup>b</sup>	Fe-2.0/CdS	4.7	4.7	--
7 <sup>a</sup>	Fe-2.0/BiVO <sub>4</sub>	3.4	2.5	0.9
8 <sup>b</sup>	Fe-2.0/BiVO <sub>4</sub>	11.1	11.1	--

Reaction conditions: a) benzyl alcohol (0.2 mmol), photocatalyst (20 mg), CH<sub>3</sub>CN (10 mL), 4Å MS (50 mg), NH<sub>3</sub> (0.1 MPa), O<sub>2</sub> balloon, 365 nm LED, 12 h, room temperature. b) maintaining the same conditions but without NH<sub>3</sub>.

In the absence of NH<sub>3</sub>, all four catalysts showed activity for the oxidation of benzyl alcohol. The conversions over Fe-2.0/TiO<sub>2</sub>, Fe-2.0/CeO<sub>2</sub>, Fe-2.0/CdS, and Fe-2.0/BiVO<sub>4</sub> were 51.5%, 35.5%, 4.7%, and 11.1%, respectively. However, in the presence of NH<sub>3</sub>, the conversions of benzyl alcohol over Fe-2.0/CeO<sub>2</sub>, Fe-2.0/CdS, and Fe-2.0/BiVO<sub>4</sub> were greatly impacted, with the highest conversion only less than 5%. While for the Fe-2.0/TiO<sub>2</sub>, the conversion of benzyl alcohol still reached 47.7%. This result reveals that when exposed to the NH<sub>3</sub> atmosphere, Fe-2.0/CeO<sub>2</sub>, Fe-2.0/CdS, and Fe-2.0/BiVO<sub>4</sub> lost their ability to activate benzyl alcohol.

**Table S4.** EXAFS fitting parameters at the Fe K-edge for various samples ( $S_0^2=0.80$ ).

Sample	Shell	CN <sup>a</sup>	R(Å) <sup>b</sup>	$\sigma^2$ (Å <sup>2</sup> ·10 <sup>-3</sup> ) <sup>c</sup>	$\Delta E_0$ (eV) <sup>d</sup>	R factor (%)
<i>Fe K-edge</i>						
Fe Foil	Fe-Fe <sub>1</sub>	8*	2.44±0.006	0.0049	4.51±1.22	0.6
	Fe-Fe <sub>2</sub>	6*	2.83±0.014	0.0061	7.42±2.02	
Fe <sub>2</sub> O <sub>3</sub>	Fe-O <sub>1</sub> *	3*	1.93±0.012	0.0065	3.64±0.25	1.0
	Fe-O <sub>2</sub> *	3*	2.07±0.020	0.0039	5.20±1.15	
FeO	Fe-O*	6*	2.14±0.023	0.0050	0.85±3.20	0.7
Fe-2.0/TiO <sub>2</sub>	Fe-O	6.0±0.2	2.02±0.007	0.0075	7.32±0.92	0.6
	Fe-O-Fe	2.0±0.1	3.06±0.011	0.0071	0.94±1.25	
Fe-2.0/TiO <sub>2</sub> -H <sub>2</sub> SO <sub>4</sub>	Fe-O	5.7±0.3	2.02±0.007	0.0094	9.21±0.93	0.5

<sup>a</sup>CN, coordination number; <sup>b</sup>R, the distance between absorber and backscatter atoms; <sup>c</sup> $\sigma^2$ , Debye-Waller factor to account for both thermal and structural disorders; <sup>d</sup> $\Delta E_0$ , inner potential correction; R factor indicates the goodness of the fit.  $S_0^2$  was fixed to 0.80, according to the experimental EXAFS fit of Fe foil by fixing CN as the known crystallographic value.

**Table S5.** Control experiments with or without NH<sub>3</sub> in the presence of HAT agents.

Entry	HAT	Yield of products (%)		
		Benzaldehyde	Nitrile	Overoxidation
1 <sup>a</sup>	NH <sub>4</sub> F	4.4	76.2	N.D.
2 <sup>b</sup>	NH <sub>4</sub> F	9.5	4.5	81.1
3 <sup>a</sup>	NH <sub>4</sub> Cl	3.4	71.6	N.D.
4 <sup>b</sup>	NH <sub>4</sub> Cl	6.4	2.4	85.3
5 <sup>a</sup>	NH <sub>4</sub> Br	Trace	99.0	N.D.
6 <sup>b</sup>	NH <sub>4</sub> Br	7.3	9.3	79.0
7 <sup>a</sup>	KBr	4.1	78.5	N.D.
8 <sup>b</sup>	KBr	11.2	N.D.	81.2

Reaction conditions: a) benzyl alcohol (0.2 mmol), photocatalyst Fe-2.0/TiO<sub>2</sub> (20 mg), CH<sub>3</sub>CN (10 mL), 4Å MS (50 mg), NH<sub>3</sub> (0.1 MPa), O<sub>2</sub> balloon, 365 nm LED, 24 h, room temperature. b) maintaining the same conditions but without NH<sub>3</sub>.

**Table S6.** The Fe iron contents in the fresh Fe-2.0/TiO<sub>2</sub> catalyst, the Fe-2.0/TiO<sub>2</sub> catalyst collected after irradiated for 2 weeks, the Fe-2.0/TiO<sub>2</sub> catalyst collected after being recycled 5 times, and the Fe-2.0/TiO<sub>2</sub>-H<sub>2</sub>SO<sub>4</sub> sample measured by ICP-AES.

Catalyst	Fresh Fe-2.0/TiO <sub>2</sub>	Irradiated for 2 weeks	Recycled 5 times	Fe-2.0/TiO <sub>2</sub> -H <sub>2</sub> SO <sub>4</sub>
Fe content (wt%)	1.872	1.866	1.858	0.586

We performed ICP characterization of the catalyst after long-term irradiation (2 weeks) and recycling to determine iron attrition. The iron content of the fresh catalyst was 1.872%, which did not change much after it was recycled five-time (1.866%) or when it was irradiated for two weeks (1.858%). In both cases, the iron loss was less than 0.01%. This proves that the photocatalyst is stable for long-term irradiation and is capable of being recycled. The Fe content in Fe-2.0/TiO<sub>2</sub>-H<sub>2</sub>SO<sub>4</sub> is 0.586 wt%, which is lower than that of the fresh one (1.872 wt%), indicating that iron species were partially removed. Moreover, no iron oxide particles were observed in the HR-TEM images of Fe-2.0/TiO<sub>2</sub>-H<sub>2</sub>SO<sub>4</sub> (**Figure S7, d-f**), and the EXAFS spectrum of Fe-2.0/TiO<sub>2</sub>-H<sub>2</sub>SO<sub>4</sub> discloses the disappearance of Fe-O-Fe bond after acid treatment (**Figure 3**). These results confirm that only doped Fe in the TiO<sub>2</sub> survived in the Fe-2.0/TiO<sub>2</sub>-H<sub>2</sub>SO<sub>4</sub> sample. In principle, the possible leaching processes of Fe species by acid treatment and during the photocatalytic process are quite different. When the fresh Fe-2.0/TiO<sub>2</sub> was washed by diluted H<sub>2</sub>SO<sub>4</sub>, the isolated FeO<sub>x</sub> species on the catalyst surface were easily dissolved, while the Fe doped in the TiO<sub>2</sub> crystal was more stable. The supplemented ICP-AES and XPS results, as well as the TEM images and XAS data, have confirmed this deduction. Potential differences between the used and fresh samples are the change in the valence of the Fe species caused by photocorrosion and the leaching by mechanical stirring. According to the ICP-AES data, the Fe contents in the recycled sample (1.858 wt%) and the sample irradiated for 2 weeks (1.866 wt%) are only slightly lower than that in the fresh sample (1.872 wt%), indicating that leaching of Fe species is not obvious during the photocatalytic process. Besides, the XPS, XRD, and TEM analysis did not show the difference in the valence of Fe between

the used samples and the fresh sample, indicating that photocorrosion is also not likely to occur rapidly in this photocatalytic system.

**Table S7.** Control experiments with or without IPA in the absence or presence of NH<sub>4</sub>Br.

<b>Substrate</b>	<b>Conditions</b>	<b>Yield of benzaldehyde (%)</b>	<b>Yield of nitrile (%)</b>
Benzyl alcohol (Without NH <sub>4</sub> Br)	No IPA	8.5	36.5
	IPA	12.1	32.8
Benzaldehyde (Without NH <sub>4</sub> Br)	No IPA	--	43.0
	IPA	--	38.9
Benzyl alcohol (With NH <sub>4</sub> Br)	No IPA	1.9	76.6
	IPA	2.8	54.8
Benzaldehyde (With NH <sub>4</sub> Br)	No IPA	--	98.0
	IPA	--	81.8

**Table S8.** Band structures of TiO<sub>2</sub>, Fe-0.3/TiO<sub>2</sub>, Fe-1.1/TiO<sub>2</sub>, Fe-2.0/TiO<sub>2</sub>, and Fe-6.0/TiO<sub>2</sub> calculated from the UV–vis absorption spectra and Mott-Schottky analyses.

Sample	E <sub>g</sub> (eV)	VB (eV)	CB (eV)
TiO <sub>2</sub>	3.24	2.66	-0.58
Fe-0.3/TiO <sub>2</sub>	3.13	2.61	-0.52
Fe-1.1/TiO <sub>2</sub>	3.11	2.59	-0.52
Fe-2.0/TiO <sub>2</sub>	3.09	2.60	-0.49
Fe-6.0/TiO <sub>2</sub>	2.99	2.41	-0.58

Combining the bandgap energies calculated from the optical absorption (**Figure S6b**), we determined the valence band energies of TiO<sub>2</sub> and Fe-*x*/TiO<sub>2</sub> samples (**Table S8 and Figure S6d**). The valence band energy of Fe-*x*/TiO<sub>2</sub> samples, except the Fe-6.0/TiO<sub>2</sub> sample, became slightly less positive compared to TiO<sub>2</sub>, suggesting that the modification with Fe(III) slightly weakened the photocatalytic oxidation power. This is consistent with the observation that the alcohol conversion over the Fe-*x*/TiO<sub>2</sub> samples (except Fe-6.0/TiO<sub>2</sub>) is like that over TiO<sub>2</sub> (**Table 1**). Sufficient aerobic oxidation power is critical for this photocatalytic synthesis. The valence band decrease in the Fe-6.0/TiO<sub>2</sub> sample is ascribed to the valence band co-dominated by TiO<sub>2</sub> and  $\alpha$ -Fe<sub>2</sub>O<sub>3</sub>.



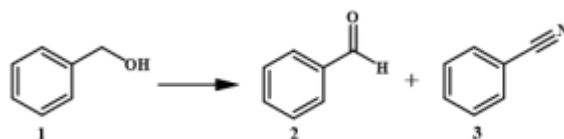
**Table S9.** Screening of semiconductors photocatalysts and transition metal dopants.

<b>Entry</b>	<b>Photocatalyst</b>	<b>Yield (%)</b>
1	Fe-2.0/ TiO <sub>2</sub>	36.6
2	Co-2.0/TiO <sub>2</sub>	16.3
3	Ni-2.0/TiO <sub>2</sub>	3.2
4	Cu-2.0/TiO <sub>2</sub>	5.7
5	Fe-2.0/CeO <sub>2</sub>	1.9
6	Fe-2.0/CdS	N.D.
7	Fe-2.0/BiVO <sub>4</sub>	2.5

Reaction conditions: benzyl alcohol (0.2 mmol), photocatalyst (20 mg), CH<sub>3</sub>CN (10 mL), 4Å MS (50 mg), NH<sub>3</sub> (0.1 MPa), O<sub>2</sub> balloon, 365 nm LED, 12 h, room temperature.

TiO<sub>2</sub> was also modified with other transition metals (Co, Ni, Cu) using the same procedure as Fe-2.0/TiO<sub>2</sub> and screened for the same reaction. Only Co-2.0/TiO<sub>2</sub> delivered a higher benzonitrile yield than pristine TiO<sub>2</sub> but was still much lower than Fe-2.0/TiO<sub>2</sub> (16.3% vs 36.6%). A possible reason for this is that incorporating these metal ions into the crystal lattice of TiO<sub>2</sub> is more difficult than Fe<sup>3+</sup> ions. We also found that other common iron-modified semiconductors (CeO<sub>2</sub>, CdS, and BiVO<sub>4</sub>) exhibited poor conversions for this transformation.

**Table S10.** Optimization of solvent for the ammoxidation of benzyl alcohol to benzonitrile over Fe-2.0/TiO<sub>2</sub>.



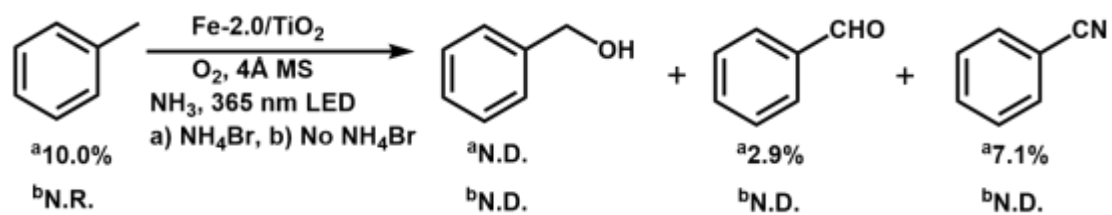
Entry	Solvent	Conv.(%)	Sel. of nitrile (%)
1	CH <sub>3</sub> CN	49.6	73.8
2	DMF	43.4	52.3
3	THF	32.6	49.7
4	EtOH	23.1	35.5
5	Benzotrifluoride	41.6	65.3

Reaction conditions: benzyl alcohol (0.2 mmol), Fe-2.0/TiO<sub>2</sub> (20 mg), solvent (10 mL), 4Å MS (50 mg), NH<sub>3</sub> (0.1 MPa), O<sub>2</sub> balloon, 365 nm LED, 12 h, room temperature.

Acetonitrile was the best reaction solvent, while other solvents had lower conversions or product selectivity.

### 3. Supporting Scheme.

**Scheme 1.** Control experiments using toluene as substrate with or without  $\text{NH}_4\text{Br}$ .



## References

- 1 J. Xie, R. Jin, A. Li, Y. Bi, Q. Ruan, Y. Deng, Y. Zhang, S. Yao, G. Sankar, D. Ma, J. Tang. Highly selective oxidation of methane to methanol at ambient conditions by titanium dioxide-supported iron species. *Nat. Catal.* **2018**, 1, 889-896.
- 2 D. Jiang, Z. Sun, H. Jia, D. Lu, P. Du. A cocatalyst-free CdS nanorod/ZnS nanoparticle composite for high-performance visible-light-driven hydrogen production from water. *J. Mater. Chem. A.* **2016**, 4, 675-683.
- 3 L. N. Chen, K. P. Hou, Y. S. Liu, Z. Y. Qi, Q. Zheng, Y. H. Lu, J. Y. Chen, J. L. Chen, C. W. Pao, S. B. Wang, Y. B. Li, S. H. Xie, F. D. Liu, D. Prendergast, L. E. Klebanoff, V. Stavila, M. D. Allendorf, J. Guo, L. S. Zheng, J. Su, G. A. Somorjai. Efficient Hydrogen Production from Methanol Using a Single-Site Pt<sub>1</sub>/CeO<sub>2</sub> Catalyst. *J. Am. Chem. Soc.* **2019**, 141, 17995-17999.
- 4 Y. Wang, G. Tan, T. Liu, Y. Su, H. Ren, X. Zhang, A. Xia, L. Lv, Y. Liu. Photocatalytic properties of the g-C<sub>3</sub>N<sub>4</sub>/010 facets BiVO<sub>4</sub> interface Z-Scheme photocatalysts induced by BiVO<sub>4</sub> surface heterojunction. *Appl. Catal. B: Environ.* **2018**, 234, 37-49.
- 5 G. Cheng, X. Liu, X. Song, X. Chen, W. Dai, R. Yuan, X. Fu. Visible-light-driven deep oxidation of NO over Fe doped TiO<sub>2</sub> catalyst: Synergic effect of Fe and oxygen vacancies. *Appl. Catal. B: Environ.* **2020**, 277, 119196.
- 6 Sołtys-Mróz, M.; Syrek, K.; Pierzchała, J.; Wiercigroch, E.; Malek, K.; Sulka, G. D., Band gap engineering of nanotubular Fe<sub>2</sub>O<sub>3</sub>-TiO<sub>2</sub> photoanodes by wet impregnation. *Appl. Surf. Sci.* **2020**, 517 (2020), 146195.
- 7 Sarkar, A.; Khan, G. G., The formation and detection techniques of oxygen vacancies in titanium oxide-based nanostructures. *Nanoscale* **2019**, 11 (8), 3414-3444.
- 8 C. Xu, P. Ravi Anusuyadevi, C. Aymonier, R. Luque, S. Marre. Nanostructured materials for photocatalysis. *Chem. Soc. Rev.* **2019**, 48, 3868-3902.
- 9 J. He, L. Chen, D. Ding, Y.-K. Yang, C.-T. Au, S.-F. Yin. Facile fabrication of novel Cd<sub>3</sub>(C<sub>3</sub>N<sub>3</sub>S<sub>3</sub>)<sub>2</sub>/CdS porous composites and their photocatalytic performance for toluene selective oxidation under visible light irradiation. *Appl. Catal. B: Environ.* **2018**, 233, 243-249.